



# Correlated XANES, TEM, and NanoSIMS of presolar graphite grains

Evan E. Groopman<sup>a,b,c,\*</sup>, Larry R. Nittler<sup>d</sup>

<sup>a</sup> *Laboratory for Space Science, Washington University in St. Louis, One Brookings Drive, St. Louis, MO 63130, USA*

<sup>b</sup> *National Research Council Postdoctoral Fellow at the U.S. Naval Research Laboratory, 4555 Overlook Avenue SW, Washington, DC 20375, USA*

<sup>c</sup> *Materials Science and Technology Division, U.S. Naval Research Laboratory, 4555 Overlook Avenue SW, Washington, DC 20375, USA*

<sup>d</sup> *Department of Terrestrial Magnetism, Carnegie Institution of Washington, 5251 Broad Branch Rd NW, Washington, DC 20015, USA*

Received 26 October 2016; accepted in revised form 8 February 2017; available online 20 February 2017

## Abstract

We report correlated XANES, TEM, and NanoSIMS measurements of twelve presolar graphite grains extracted from primitive meteorites and for which isotopic data indicate predominantly Type-II supernovae origins. We find continued evidence for isotopic heterogeneities in presolar graphite grains, including the first observation of a radial gradient in the inferred initial  $^{26}\text{Al}/^{27}\text{Al}$  within a presolar graphite grain. The XANES spectra of these samples show a variety of minor absorbances near the C K-edge, attributable to vinyl-keto, aliphatic, carboxyl, and carbonate molecules, as well as possible damage during sample preparation. Each sample exhibits homogeneous C K-edge XANES spectra within the graphite, however, showing no correlation with isotopic heterogeneities. Gradients in the isotope ratios of C, N, O, and Al could be due to both processes during condensation, e.g., mixing in stellar ejecta and granular transport, and post-condensation effects, such as isotope dilution and exchange with isotopically normal material in the early Solar System or laboratory, the latter of which is a significant issue for high-density presolar graphite grains. It remains unknown whether the mechanisms behind isotope exchange would also affect the local chemistry and therefore the XANES spectra. Ti L-edge XANES from most Ti-rich subgrains match standard spectra for TiC and potentially TiCN. A rare rutile ( $\text{TiO}_2$ ) subgrain has been identified, though it lacks the lowest energy  $L_3$  peak typically seen in standard spectra. Ca has also been identified by EDXS in TiC subgrains, likely due to the decay of live  $^{44}\text{Ti}$  at the time of formation. Future NanoSIMS measurements will determine the variability of initial  $^{44}\text{Ti}$  in TiC subgrains, an important constraint on mixing in the ejecta of the grains' parent supernovae.

Published by Elsevier Ltd. This is an open access article under the CC BY license (<http://creativecommons.org/licenses/by/4.0/>).

**Keywords:** Presolar grains; Stardust; Supernovae; NanoSIMS; XANES; TEM; Nucleosynthesis; Meteorites

## 1. INTRODUCTION

Presolar grains of stardust are found in primitive extraterrestrial materials including meteorites and cometary dust (Zinner, 2014). They condensed in the ejecta and/or

outflows of evolved stellar objects, including supernovae (SN), asymptotic giant branch (AGB) stars, novae, and born-again AGB stars. As stellar condensates, presolar grains are micron- and sub-micron-sized time capsules of their parent stars' nucleosynthetic products and physiochemical environments and they provide a wide range of information for astrophysics and cosmochemistry. The most significant advances to presolar grain research have come through the use of Secondary Ion Mass Spectrometry (SIMS/NanoSIMS) to measure the elemental and isotopic

\* Corresponding author at: Materials Science and Technology Division, U.S. Naval Research Laboratory, Washington, DC 20375, USA.

E-mail address: [evan.groopman@nrl.navy.mil](mailto:evan.groopman@nrl.navy.mil) (E.E. Groopman).

compositions of individual grains (e.g., Zinner et al., 1987, 1995; Amari et al., 1990; Hutcheon et al., 1994; Nittler et al., 1994; Messenger et al., 2003) combined with models of stellar nucleosynthesis (e.g., Gallino et al., 1994; Woosley and Weaver, 1995; Rauscher et al., 2002; Cristallo et al., 2011); and Transmission Electron Microscopy (TEM) studies of the grains' internal structures and subgrain contents (e.g., Bernatowicz et al., 1987, 1996; Daulton et al., 1996; Croat et al., 2003; Stroud et al., 2004) combined with models of condensation in stellar atmospheres (e.g., Lodders and Fegely, 1995; Fedkin et al., 2010). These techniques and models not only identify and characterize individual presolar grains, but identify the class of progenitor star and even regions from within the parent star that each grain's material originated. Numerous other techniques have yielded invaluable presolar grain information, including scanning electron microscopy, noble-gas mass spectrometry, resonance ionization mass spectrometry, Raman spectroscopy, and X-ray fluorescence. Given each presolar grain's small size and uniqueness, the most powerful studies combine many techniques into a coordinated series of analyses to maximize the information obtained from each grain. Scanning Transmission X-ray Microscopy (STXM) is one more non-destructive technique, which can be added to the arsenal of presolar grain research techniques.

STXM and X-ray absorption near-edge structure (XANES) microspectroscopy are synchrotron-based techniques complementary to TEM, as they are essentially non-destructive and require no additional preparation. Individual and correlated XANES, NanoSIMS, and TEM studies have been carried out on extraterrestrial cometary material from NASA's STARDUST mission (Cody et al., 2008; Matrajt et al., 2008; De Gregorio et al., 2010, 2011), and meteorite organics (Herd et al., 2011; De Gregorio et al., 2013; Le Guillou et al., 2014) with XANES analyses focused on C, N, and O K-edge absorption spectra. Ti L-edge XANES absorption features of presolar grains, including hibonite ( $\text{CaAl}_2\text{O}_9$ ) (Zega et al., 2012) and TiC inclusions within graphite grains (Groopman et al., 2012b) have also been reported. Many other carbonaceous samples have been probed using C-XANES, including terrestrial graphite, e.g., (Bruhwiler et al., 1995; Ahuja et al., 1996; Brandes et al., 2008), interplanetary dust particles (IDPs) (Flynn et al., 2003, 2013; Keller et al., 2004), meteorite matrix from carbonaceous chondrites (Kebukawa et al., 2014), carbonaceous grains from asteroid Itokawa (Yabuta et al., 2014), and kerogens and coals, e.g., (Cody et al., 1995).

A wide variety of presolar grain types have been identified including silicates, oxides, SiC, diamond, and graphite, the latter a convenient shorthand for elemental carbon spanning a range of crystallinities, from poorly crystalline to turbostratic to highly ordered (Zinner, 2014). Here we report on C, N, O, and Ti-XANES measurements of eleven low-density and one high-density presolar graphite grains from the Murchison and Orgueil meteorites. Low-density (LD) graphite grains ( $\rho = 1.60\text{--}2.05 \text{ g cm}^{-3}$ ; (Amari et al., 1994; Jadhav et al., 2006)) have been identified as condensates from Type-II SN explosions, while high-density (HD) graphite grains ( $\rho > 2.05 \text{ g cm}^{-3}$ ;  $\rho = 2.09\text{--}2.23 \text{ g cm}^{-3}$  for

pure graphite) generally condensed around AGB stars and SNe (Amari et al., 1995; Hoppe et al., 1995; Zinner et al., 1995; Bernatowicz et al., 1996; Jadhav et al., 2006). Morphologically, both populations of grains are quasi-spherical (Zinner et al., 1990; Amari et al., 1994), though HD grains typically consist of concentric shells of highly ordered graphite, "onions" (Bernatowicz et al., 1996; Croat et al., 2005), while LD grains are characterized by turbostratic graphite, "cauliflowers", with planar stacking distances up to 5% larger than ideal graphite (Croat et al., 2003, 2008). Correlated isotopic, chemical, and structural studies have proven to provide the most comprehensive compositional information of presolar graphite grains (e.g., Croat et al., 2003; Bernatowicz et al., 2005; Stadermann et al., 2005; Croat et al., 2010), which may be related to the properties of the stellar ejecta.

One of the outstanding questions regarding presolar graphite grains is the extent to which isotope dilution and exchange following condensation affects their isotopic compositions. Heterogeneities in the isotopic compositions of presolar graphite grains have been attributed both to primary processes during condensation, such as mixing of stellar ejecta and granular transport, and to secondary post-condensation processes, potentially attributable to wet chemistry in the lab or alteration of the meteorite host rock (Stadermann et al., 2005; Groopman et al., 2012a, 2014). The high-density presolar graphite grains from AGB stars are particularly problematic, as they often have terrestrial N and O isotopic compositions, far from their expected compositions based upon their highly anomalous  $^{12}\text{C}/^{13}\text{C}$  ratios (Hoppe et al., 1995; Zinner et al., 1995; Jadhav et al., 2006, 2013). This issue is less dramatic for the low-density graphite grains, which retain significant N, O, and other minor element anomalies (Zinner, 2014). One of the goals of this study is to test the viability of using XANES to examine how and if the local chemistry within the presolar graphite changes with respect to the isotopic composition.

## 2. METHODS AND SAMPLES

### 2.1. Samples

Eleven low-density (LD) and one high-density (HD) presolar graphite grains from acid residues of the Murchison (KE3; (Amari et al., 1994)) and Orgueil carbonaceous chondrite meteorites (OR1d, OR1g; (Jadhav et al., 2006)) were studied with the NanoSIMS. They were subsequently picked with a micromanipulator, potted in LR White hard resin alongside carbon fibers (for locating in the TEM and STXM), and ultramicrotomed into 70 nm-thick sections, which were deposited on holey-C and SiO coated TEM grids and Si wafers (Croat et al., 2003; Groopman et al., 2012a; Groopman et al., 2014). Most of these sections were analyzed in the TEM prior to STXM/XANES analyses (see Fig. 3 for TEM images). TEM studies of some grains have previously been reported, identifying subgrains of TiC (KE3e6, OR1d6m-6, OR1d6m-17, OR1d6m-18) (Croat et al., 2003; Groopman et al., 2012a; Groopman et al., 2014), SiC (OR1d6m-6) (Groopman et al., 2014), Fe-Ni metal (KE3e6,

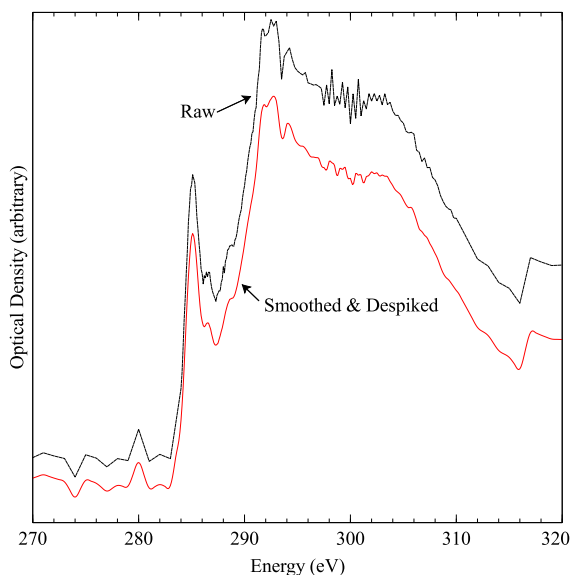


Fig. 1. Example of despiking and smoothing algorithm on C K-edge XANES spectrum from presolar graphite grain OR1d6m-23 (see text for details). Raw input spectrum (dashed) vs. smoothed output (solid, red online). (For interpretation of the references to colour in this figure legend, the reader is referred to the web version of this article.)

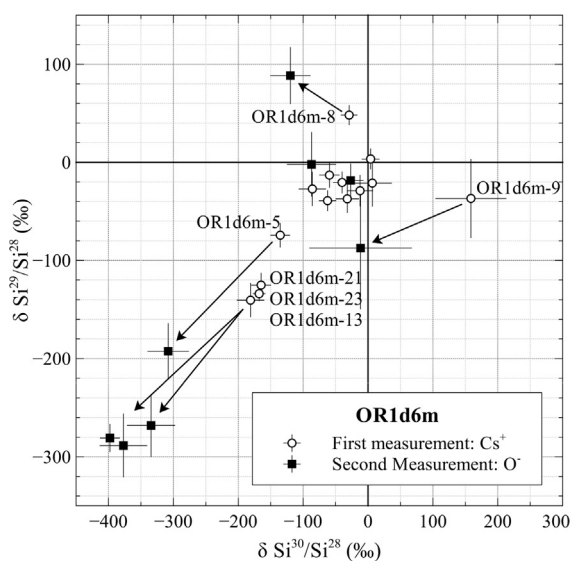


Fig. 2. Si 3-isotope  $\delta$ -value (Table 1) plot for likely presolar SN graphite grains on grain mount OR1d6m. Initial Si isotope measurements underestimate the magnitudes of the Si anomalies, likely due to residual surface contamination.

OR1d6m-6) (Croat et al., 2003; Groopman et al., 2014), and a single refractory metal nugget (OR1d6m-13) (Croat et al., 2013) though only the TiC subgrains were consistently large enough for XANES data to be extracted in this study. Fe L-edge and Mo,Ru K-edge XANES data were collected over Fe-Ni grains and the refractory metal nugget, respectively, but the signal-to-noise was too low due to the subgrains' small sizes. Approximately one third of HD gra-

phite grains contain nanocrystalline cores of randomly oriented 3–4 nm sheets of graphene (Bernatowicz et al., 1996; Croat et al., 2005), while this feature is exceedingly rare in LD grains (Groopman et al., 2014). The Groopman et al. (2014) grain, OR1d6m-6, is the only grain containing a nanocrystalline core reported on in this study.

Standards used in this study include ultramicrotomed sections of Sri Lanka (Ceylon) vein graphite, ultramicrotomed carbon fibers, and mortar-and-pestle-powdered TiC and TiN powders from ESPI Metals. The most significant challenge to using the TiC and TiN powders was producing thin enough specimens for acceptable XANES spectra to be obtained. The natural graphite sample contains impurities that would not be found in reactor grade graphite, for instance, although C K-edge XANES spectra for vein graphite has been shown to match synthetic highly ordered pyrolytic graphite (HOPG) (Brandes et al., 2008). Carbon fibers are typically synthesized from carbonaceous precursor polymers such as polyacrylonitrile (PAN;  $(C_3H_3N)_n$ ), rayon, or petroleum pitch, which are heated in successive steps to remove non-C elements and finally graphitized. Microstructurally, carbon fibers are turbostratic or graphitic depending upon their precursor material and treatment.

## 2.2. Data acquisition

TEM data were acquired on two 200 keV JEOL microscopes, a 2000FX and a 2100F, at Washington University in St. Louis. Isotopic data were acquired with the Cameca NanoSIMS 50 and ims 3f ion microprobes (only grain KE3e-6 for the latter) in the Laboratory for Space Sciences at Washington University. NanoSIMS measurement parameters are detailed in (Groopman et al., 2012a, 2014).

XANES spectra were acquired at Beamline 5.3.2.2 of the Advanced Light Source at Lawrence-Berkeley National Laboratory during seven visits between May, 2011 and April, 2015. A full description of the instrument is described in Kilcoyne et al. (2003). In brief, a small X-ray spot of  $\sim 40$  nm is produced by passing the soft X-ray beam through a zone-plate lens, e.g., a circular diffraction grating, and by selecting only the central diffraction spot with an aperture prior to the sample. A photon flux detector is positioned behind the sample. An interferometer-controlled piezoelectric stage allows for fine-scale x,y rastering of the sample relative to the stationary beam. By adjusting the spherical grating monochromator, photon energies up to 800 eV may be selected in increments as small as 0.1 eV. After each sample raster at a particular photon energy, the energy is increased generating a “stack,” a 3-dimensional image in  $x \times y \times eV$ , where each raster pixel contains a full energy spectrum. Reported energies were calibrated using  $CO_2$  gas. Raster areas were selected so that they contained regions with holes in the sample, which served as a baseline intensity,  $I_0$ . Linescans and point scans are simply special, lower-dimensional cases of the image stack. Regions containing LR White resin were avoided since this material has spectral features near the amide, carboxyl, and carbonate peaks at 288.2 eV, 288.5 eV, and 290.3 eV, respectively (Karunakaran et al., 2015). For all

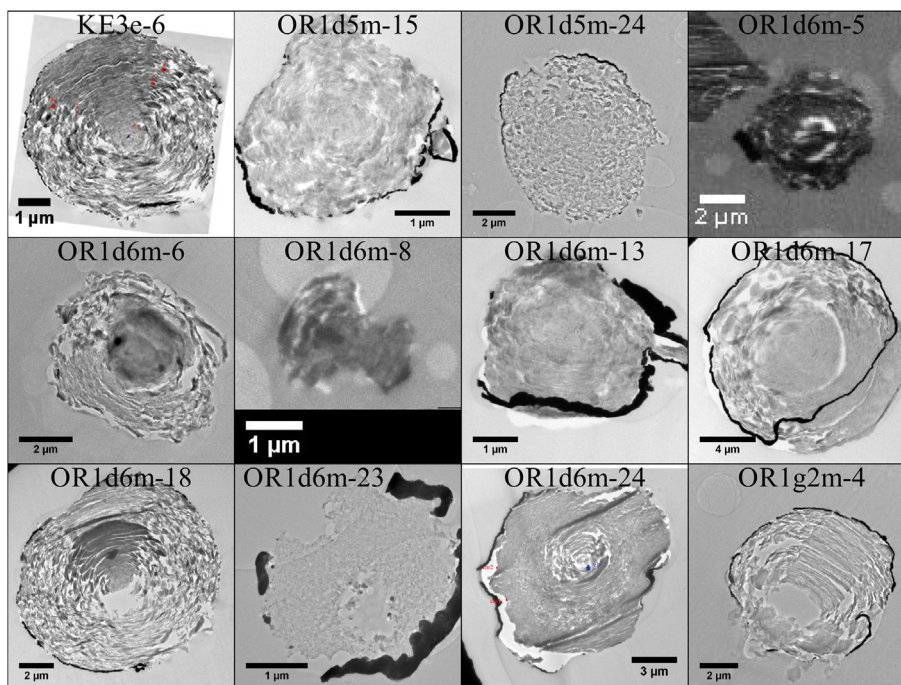


Fig. 3. Bright field TEM micrographs or STXM 300 eV absorption maps (OR1d6m-5 & 8; carbon fiber is visible in the upper left of the OR1d6m-5 image). Compression “fans” visible in KE3e-6, OR1d6m-17,-18, OR1g2m-4 are artifacts from the ultramicrotome knife. KE3e-6 image courtesy of Kevin Croat.

spectra, energy steps of 0.1 eV were used across the absorption edges, e.g., between 283 eV and 296 eV for the C K-edge, while larger 0.5 eV steps were used between different edges to save time. TEM grids were mounted over holes on small Al plates with double-sided tape. These were removed afterwards with a razor blade.

### 2.3. Data analysis

XANES spectra extraction from image stacks and linescans was performed using a home-made graphical user interface (GUI) program written in Python and Qt, inspired by Adam Hitchcock’s aXis2000 IDL program (Hitchcock, 1997–2016) and the more recent Python program MANTiS, by Mirna Lerotic (Lerotic et al., 2014). This program relies heavily on the PyQtGraph package (Campagnola, 2016) for image and data interaction along with the core scientific Python packages: Numpy (van der Walt et al., 2011), Scipy (Jones et al., 2001), scikit-learn (Pedregosa et al., 2011), and scikit-image (van der Walt et al., 2014). Similar to aXis2000 and MANTiS, the program allows for reading and writing of image stacks and linescans from various synchrotron sources, image stack alignment, region-of-interest (ROI) selection, and pixel-by-pixel principal component analysis (PCA) and clustering methods (e.g., k-means and Ward hierarchical clustering). The C-XANES spectra detailed in this report are typically the primary component from PCA – the component that explains the most variance – of the whole presolar grain section or the entire region sampled in the image stack. Where clear microstructural heterogeneities were visible, such as in grain OR1d6m-6

(Groopman et al., 2014), clustering was used to separate the different regions. Ti-XANES spectra from TiC subgrains were extracted using both PCA and clustering. Spectra from linescans were extracted by averaging over one-dimensional ROIs which were typically less than 10–15 pixels. The absorbance, or optical density (OD) of the sample, was calculated as  $OD = -\log(I/I_0)$ , where  $I$  is the intensity in each pixel and  $I_0$  is the background intensity taken through a hole in the substrate. For presolar graphite grains on holey-C-coated TEM grids, the holey-C substrate was found to negligibly contribute to the overall absorbance.

Following extraction, a linear fit to the pre-edge region was subtracted from each absorbance spectrum, e.g., 270–280 eV for C K-edge XANES spectra. Spectral spikes were identified by smoothing and differentiating each spectrum with a Savitzky-Golay filter (Savitzky and Golay, 1964) and applying an automatic Otsu threshold (Otsu, 1979) to the histogram of derivative values in a manner similar to that reported by Feuerstein et al. (2009). Each spike was replaced with linearly interpolated values from nearby points and was polynomial-smoothed across the spike width. Spectra displayed in this manuscript are smoothed using a Savitzky-Golay filter with windows between 0.7 and 1.1 eV wide for visual clarity. An example of the impact of this smoothing algorithm is shown in Fig. 1.

C K-edge  $\pi^*$  absorption peak centers were estimated by calculating the center of mass from a  $\pm 0.3$  eV window centered on the peak maximum (7 points for the standard 0.1 eV dispersion). A window size of  $\pm 0.3$  eV was chosen because it minimized the standard deviation of the derivative spectra, i.e. where the window size had the least

effect on the calculated center of mass. Qualitatively, this is a good value as it encompasses enough points across the peaks to yield a robust center of mass while not sampling too much of the  $\pi^*$  peak tail.

For the C K-edge and Ti L-edge spectra, we performed non-linear least-squares fitting in a manner similar to many other publications, (e.g., Stöhr, 1992; Cody et al., 1995; Lerotic et al., 2014). Fitting was attempted using a variety of peak and continuum step models, both with and without lifetime broadening effects, e.g., Gaussian vs. skewed normal peaks. These techniques remain unsatisfactory, however, due to their propensity to overfit the data as they include a vast number of free parameters. Markov-chain Monte Carlo fits were also attempted, though the posterior probability distributions were often not well peaked. The choice of continuum step shapes and individual peak shapes significantly affected the resulting relative peak areas. Due to the difficulty in locating global fitting extrema and the high dependence of fitting outcome on the choice of peak shapes, we do not think it appropriate to report quantitative fit results and relative peak areas. Numerous other fitting protocols exist, such as using linear combinations of standard spectra or full multiple scattering calculations, e.g., (Benfatto and Della Longa, 2001), however one principal objective of this paper is to examine the minor peaks near the C K-edge, and this complexity does not lend itself to simple modeling.

NanoSIMS images were analyzed with the custom L'Image software (L. R. Nittler, Carnegie Institution) and other in-house image processing routines.

### 3. RESULTS

Isotope ratio measurements by NanoSIMS (ims 3f for KE3e-6) are shown in Table 1. Several of these grains have been reported on in depth in earlier isotopic and microstructural studies (Croat et al., 2003; Groopman et al., 2012a;

Groopman et al., 2014, 2015). Only the original whole-grain data are reported in Table 1. The major implications of these studies should therefore be emphasized: many presolar graphite grains are not isotopically homogeneous, containing isotopic gradients in the graphite structure, and subgrains with distinct and often more anomalous isotopic compositions (Groopman et al., 2012a; Stadermann et al., 2005; Zinner and Jadhav, 2013; Groopman et al., 2014). Surface contamination naturally affects whole-grain measurements as well (Hoppe et al., 1995; Jadhav et al., 2013; Groopman et al., 2015). Since most of the data presented here were not collected in NanoSIMS ion imaging mode, the relative contribution of graphite, subgrain, and surface contaminant compositions is not known. It should also be noted that Si isotopes were measured twice with the NanoSIMS for some of the OR1d6m grains, once as Si<sup>-</sup> with a Cs<sup>+</sup> primary beam as part of the first suite of isotopes (<sup>12,13</sup>C, <sup>28,29,30</sup>Si), and also as Si<sup>+</sup> with an O<sup>-</sup> primary beam following all other measurements. We only re-measured those grains that exhibited anomalous Si from the first measurement. The second set of Si isotope measurements yielded anomalies 2 × as large as the first set, likely due to removal of surface contamination (Fig. 2).

#### 3.1. C K-Edge XANES

The signature absorption features of graphitic carbon at the K-edge are at 285.2 eV (1s → 2p  $\pi^*$  transition), a sharp peak at 291.5 eV ( $\sigma^*$  exciton), and a broader peak at 292.5 eV (also  $\sigma^*$ ) (Stöhr, 1992; Bruhwiler et al., 1995; Ahuja et al., 1996; Brandes et al., 2008). The synchrotron X-ray beam is polarized, so the amplitudes of the  $\pi^*$  peak, and to a lesser extent, the  $\sigma^*$  peaks, depend upon the orientation of the graphitic layers relative to the beam (Rosenberg et al., 1986; Stöhr, 1992; Belavin et al., 2006). The amplitude of the  $\pi^*$  peak varies as  $\sin^2(\theta)$ , where  $\theta = 0$  corresponds to an X-ray beam orthogonal to the

Table 1

Selected whole-grain isotope ratios determined by NanoSIMS and ims 3f (only KE3e-6). Bold values indicate larger than 2 $\sigma$  deviation from terrestrial. “–” indicates no data. <sup>26</sup>Al/<sup>27</sup>Al initial ratios inferred from the overabundance of <sup>26</sup>Mg relative to Solar. Parts per thousand deviation from standard isotope ratios are expressed in delta-notation:  $\delta^i\text{Si} = 1000 \times ((^i\text{Si}/^{28}\text{Si})_{\text{sample}} / (^i\text{Si}/^{28}\text{Si})_{\text{standard}} - 1)$ .

Sample	<sup>12</sup> C/ <sup>13</sup> C	1 $\sigma$	<sup>14</sup> N/ <sup>15</sup> N	1 $\sigma$	<sup>16</sup> O/ <sup>18</sup> O	1 $\sigma$	$\delta^{29}\text{Si}$	1 $\sigma$	$\delta^{30}\text{Si}$	1 $\sigma$	<sup>26</sup> Al/ <sup>27</sup> Al ( $\times 10^{-2}$ ) <sup>†</sup>	1 $\sigma$ ( $\times 10^{-3}$ )	Ref.
Terrestrial	89		272		499		0		0		0		
KE3e-6	<b>231.0</b>	1.9	–	–	<b>290.2</b>	11.9	–1	32	–11	32	–	–	[1]
OR1d5m-15	<b>18.5</b>	0.3	<b>205.9</b>	4.1	<b>407.5</b>	7.2	–41	26	–64	19	–	–	
OR1d5m-24	<b>318.0</b>	4.8	<b>229.4</b>	4.5	<b>306.3</b>	5.1	2	26	–21	16	–	–	
OR1d6m-5	<b>45.9</b>	0.3	<b>248.0</b>	10.7	<b>323.5</b>	5.7	–193	29	–308	32	<b>1.8</b>	0.4	
OR1d6m-6	<b>113.2</b>	0.8	<b>145.3</b>	5.4	<b>163.2</b>	2.8	–13	13	–60	16	<b>50</b>	3.0	[2,3]
OR1d6m-8	<b>127.8</b>	0.9	<b>145.0</b>	9.3	<b>280.4</b>	5.0	<b>88</b>	29	–120	31	<b>7.7</b>	0.9	
OR1d6m-13	<b>66.0</b>	0.4	263.0	5.8	<b>170.1</b>	3.2	–288	32	–377	37	<b>35</b>	15	[3]
OR1d6m-17	<b>306.1</b>	2.1	<b>215.1</b>	10.4	<b>306.3</b>	6.4	–27	18	–87	21	<b>5.6</b>	1.7	[4]
OR1d6m-18	<b>121.0</b>	0.8	<b>148.8</b>	14.6	<b>432.9</b>	9.2	–12	16	–29	13	<b>1.2</b>	0.2	[4]
OR1d6m-23	<b>73.7</b>	0.5	<b>214.4</b>	13.1	<b>394.4</b>	7.2	–281	14	–398	15	<b>13</b>	7.7	[3]
OR1d6m-24	<b>13.1</b>	0.1	<b>236.3</b>	16.5	479.2	9.4	3	11	4	14	–	–	[4]
	<sup>12</sup> C/ <sup>13</sup> C	1 $\sigma$	$\delta^{46}\text{Ti}$	1 $\sigma$	$\delta^{47}\text{Ti}$	1 $\sigma$	$\delta^{49}\text{Ti}$	1 $\sigma$	$\delta^{29}\text{Si}$	1 $\sigma$	$\delta^{30}\text{Si}$	1 $\sigma$	
OR1g2m-4	<b>77.8</b>	0.3	<b>243</b>	66	32	63	<b>2230</b>	90	–67	29	–48	25	

Notes: † Corrected inferred initial <sup>26</sup>Al/<sup>27</sup>Al ratios for OR1d6m-6,13,23 reported in (Groopman et al., 2015).

References: [1] Croat et al. (2003), [2] Groopman et al. (2014), [3] Groopman et al. (2015), [4] Groopman et al. (2012a).

stacking direction and where the axis off which  $\theta$  is measured is parallel to the polarization direction.

Fig. 4a shows characteristic C K-edge XANES spectra from each of the twelve presolar graphite grains in this study, in addition to spectra from the Ceylon graphite and carbon fiber standards. The two spectra from Ceylon graphite illustrate the effect of sample orientation on the  $\pi^*$  and, to a lesser extent,  $\sigma^*$  peaks. Table 2 summarizes the peaks present near the C K-edge, not including  $\sigma^*$  peaks. X's indicate where a peak is clearly present by visual inspection; ?'s indicate a small or ambiguous peak; and “–” signifies no peak. All of the samples exhibit strong aromatic  $\pi^*$  resonances near 285.2 eV, as expected for graphitic carbon. All three standards have  $\pi^*$  peaks centers at 285.2 eV, while the presolar graphite grains have  $\pi^*$  peaks ranging

from 285.1 eV to 285.45 eV, with a standard deviation of 0.1 eV across all presolar samples. Between 2 and 6 samples exhibit vinyl-keto (286.5 eV); 8–12 aliphatic (287.3–288.1 eV); 8–9 carboxyl (288.4–288.7 eV); and 1–4 carbonate (290.3 eV) resonances. For the majority of the potential vinyl-keto and carbonate resonances, the ambiguity arises from the difficulty in distinguishing between broadening of the aromatic  $\pi^*$  peak tail (for the former) and broadening of the  $\sigma^*$  peak pre-edge (for the latter). Disruption of the graphite structure (e.g., from ultramicrotomy) has also been shown to cause a peak at 288.4 eV due to interlayer bonding of poorly aligned sheets (Fischer et al., 1991). This feature complicates the identification of carboxyl peaks and neighboring aliphatic peaks, as even pure graphite can exhibit a broad absorption peaked at 288.4 eV (see

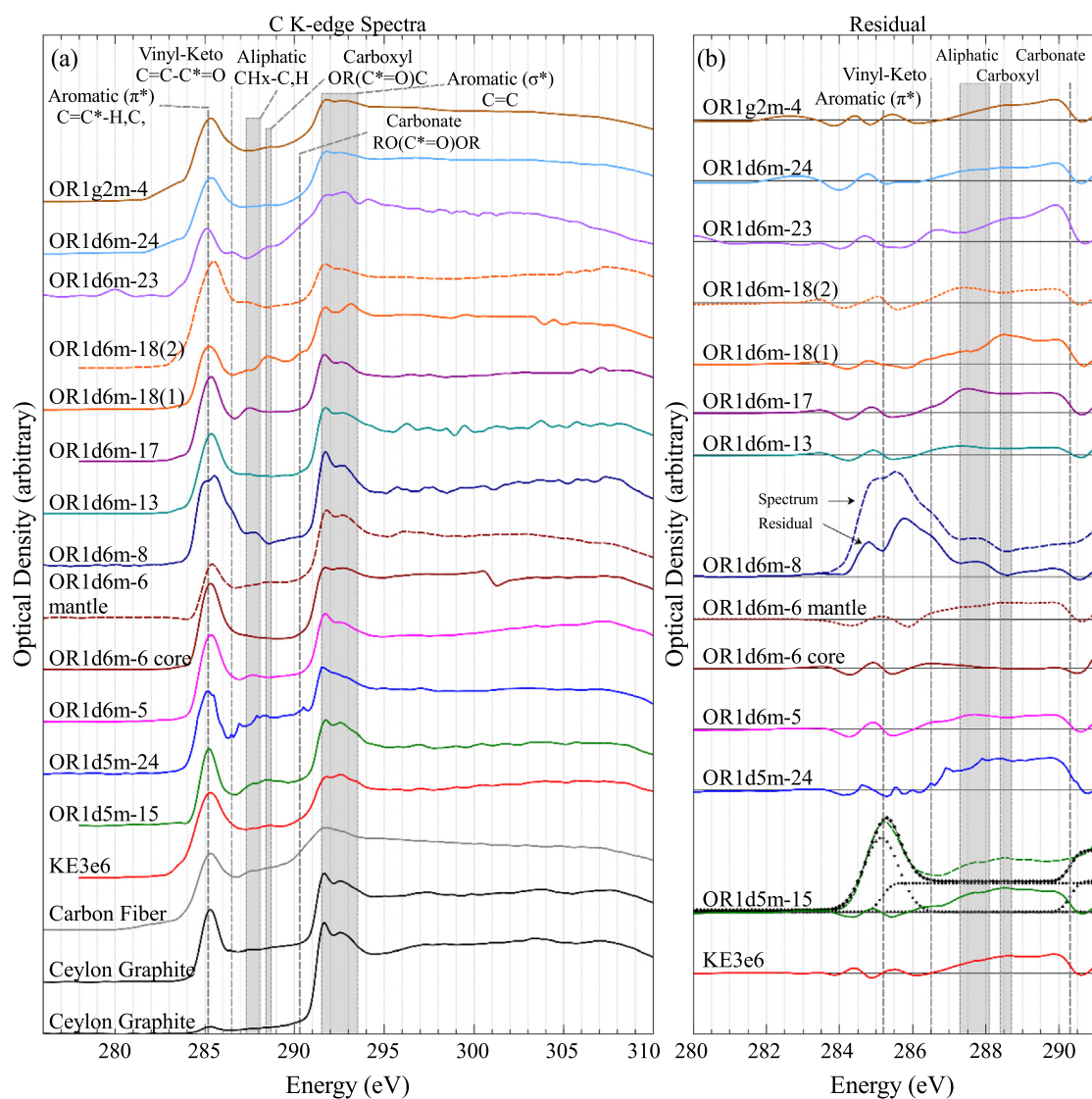


Fig. 4. (a) C K-edge XANES spectra of presolar grains and standards. Two different orientations are shown for Ceylon vein-ore graphite. (b) Residual spectra enhancing qualitative differences. Residuals calculated by fitting a Gaussian or skewed Gaussian profile plus erf step function to the aromatic  $\pi^*$  peak and adding a step for aromatic C at 290.3 eV. OR1d5m-15 profile shows original spectrum (green dashed), fit components (symbols), fit total (symbols + line), and residual (green solid). (For interpretation of the references to colour in this figure legend, the reader is referred to the web version of this article.)

Table 2  
Summary of peaks near C K-edge.

Sample	Aromatic (285.2 eV)	Vinyl-Keto (286.5 eV)	Aliphatic (287.3–288.1 eV)	Carboxyl (288.4–288.7 eV)	Carbonate (290.3 eV)
Ceylon ( $\theta < 10^\circ$ )	X	–	?	–	–
Ceylon ( $\theta > 30^\circ$ )	X	?	?	–	–
Carbon Fiber	X	–	X	?	?
KE3e6C5	X	–	–	X	–
OR1d5m-15	X	–	X	X	–
OR1d5m-24	X	–	X	X	?
OR1d6m-5	X	–	X	–	–
OR1d6m-6 core	X	–	–	–	–
OR1d6m-6 mantle	X	–	?	X	–
OR1d6m-8	X	X	X	–	–
OR1d6m-13	X	–	X	–	–
OR1d6m-17	X	–	X	–	–
OR1d6m-18 (1)	X	–	?	X	X
OR1d6m-18 (2)	X	–	X	–	–
OR1d6m-23	X	X	–	X	?
OR1d6m-24	X	?	–	X	–
OR1g2m-4	X	?	–	X	–
<b>Total</b>	17	2–6	8–12	8–9	1–4

Brandes et al. (2008) Fig. 2). Sample preparation by ultramicrotomy seems likely to contribute to the presence of the disruption-induced peaks in the spectra, however these may also be due to the turbostratic nature of the LD presolar graphite. Hereafter, we refer to changes induced in the XANES spectra by sample preparation as “section damage.” The carbon fiber spectrum is graphitic, though it lacks the well-defined  $\sigma^*$  peaks of Ceylon graphite and also contains a minor peak in the aliphatic range, perhaps due to incomplete graphitization of the precursor polymer.

Background-subtracted residual spectra are shown in Fig. 4b. Instead of full spectral fitting, an ideal graphite spectrum was simulated and subtracted from each sample spectrum based upon the relative magnitudes of its  $\pi^*$  and  $\sigma^*$  peaks. Following a suggestion by Stöhr (1992), we modeled the  $\pi^*$  peak and plateau region up to 5 eV above the  $\pi^*$  peak as a Gaussian plus an error function (erf) step centered on the Gaussian profile. The absorbance modeled by the step function under the  $\pi^*$  peak is potentially due to multielectron excitations (Stöhr, 1992). For simplicity we did not include a separate component for the C 1s- $2\pi^*$  transition near 289 eV, which has been found to be roughly  $\frac{1}{4}$  of the intensity of the primary  $\pi^*$  transition (Francis and Hitchcock, 1992). This model provided a good fit to our graphite standard spectra. Using our own Ceylon Graphite spectra and data kindly provided by Jay Brandes from Brandes et al. (2008), we determined that the relative amplitude ratio of the underlying step to the Gaussian  $\pi^*$  peak is  $0.33 \pm 0.03$ . At least to first order, the plateau amplitude/ $\pi^*$  ratio is linear across a wide range of planar orientations, with an intercept through the origin, within errors. For each sample spectrum, a Gaussian or skewed Gaussian profile was fit to the  $\pi^*$  peak and an erf step function centered under the Gaussian was added with a relative amplitude of 0.33 and a width of 1 eV. A similar step profile was added at the aromatic vacuum level (290.3 eV). These profiles were fit to the data, omitting the region between 286 and

290.5 eV, where all of the minor C K-edge peaks reside. Removing this model background from the sample spectrum allows for an enhanced comparison between the sample spectra. Fig. 4b (OR1d5m-15) illustrates the individual components of each background fit. Due to the simplistic nature of the chosen “ideal” background for each spectrum, some peaks are emphasized relative to others. Other peaks, such as carbonate, are minimized and therefore are hardly apparent in the residual spectra. The primary goal of this background subtraction is therefore to emphasize the differences between the presolar grain spectra, even if these spectra are not quantitative.

Phi coefficients ( $\phi$ , equivalent to the Pearson r correlation coefficient for binary data) were calculated between the set of minor peaks present in the samples. Since the presence of numerous peaks was ambiguous, coefficients were calculated at each extreme: either accepting or rejecting all ?'s. Most comparisons yielded no correlation among the grain spectra. For the case of accepting all potential peaks (?'s), the presence of carboxyl and carbonate peaks was positively correlated ( $\phi = 0.52$ ,  $p = 0.03$ ), while the presence of vinyl-keto and aliphatic resonances are weakly anticorrelated ( $\phi = -0.43$ ,  $p$ -value = 0.08). Weak anticorrelation was calculated between aliphatic and carboxyl resonances when rejecting all ?'s ( $\phi = -0.42$ ,  $p = 0.10$ ) and accepting all ?'s ( $\phi = -0.35$ ,  $p = 0.17$ ), though neither of these are statistically significant. If the Gaussian curve fitting procedures yielded more reliable and unique results for each spectrum, the true presence of each peak could be inferred. As it stands, the correlations between the presence of particular peaks are likely less than the values given here, though still significant. Since reliable O and H abundance data is not available for these samples, it is difficult to know whether these correlations simply represent differences in elemental concentrations within the samples. As described above, the potential presence of absorbances due to disrupted graphite also confound these correlations.

However, due to the variety of minor resonances in the presolar graphite grain spectra and the uniform sample preparation procedures, it is unlikely that all of the minor resonances are due to sample preparation or laboratory alteration of the material. We can tentatively conclude that the (anti)correlated presence of vinyl-keto and aliphatic excitons, and carboxyl and carbonate excitons, reflect heterogeneous processes such as different grain formation conditions in the parent stars. In comparison to the variety of features are the C K-edge, the N and O K-edge XANES spectra for most of the presolar graphite grains are unremarkable, consisting of small dome-like resonances, if present at all. Exceptions are discussed below.

### 3.2. Ti standards

Characteristic C K-edge and Ti L-edge spectra from our TiC standard are shown in Fig. 5a. These spectra are similar to electron energy loss spectra (EELS) shown by Paxton et al. (2000) (see their Fig. 4b), though they contain more fine structure. The C K-edge is characterized by either a sharp peak at 285 eV, a shoulder around 284 eV, and peaks near 286.5 and 287.5 eV; or by a larger absorption at 284 eV with a shoulder to lower energy, plus the other aforementioned peaks to higher energy. The Ti L-edge has split  $L_3$  peak and either a single broad or mildly split  $L_2$  peak. Each different characteristic C K-edge and Ti L-edge spectrum characterizes approximately half of the measured TiC grains. There is no apparent correlation between the minor differences in the Ti L-edge features and the more distinctive C K-edge differences. Characteristic N K-edge and Ti L-edge spectra for our TiN standard are shown in Fig. 5b. These also match those in Paxton et al. (2000) Fig. 5, and exhibit little spot-to-spot variation. Two broad absorptions characterize both the N K- and Ti L-edges with no fine splitting. Fig. 5c shows characteristic Ti L-edge XANES for TiO<sub>2</sub> (rutile), with significant and well-defined splitting in the  $L_3$  and  $L_2$  peaks, from Zega et al. (2012).

### 3.3. Individual Presolar Grain Results

#### 3.3.1. KE3e-6

Presolar graphite grain KE3e-6 has a likely SN origin and exhibits a carboxyl peak at its C K-edge (Fig. 4a). The aromatic  $\pi^*$  peak appears wider than those from other grains and standards. KE3e-6 is one of the few graphite grains that exhibits complex N and O spectra in both its Ti-rich subgrains and within the graphite structure itself. Fig. 6a shows an absorbance contrast image of KE3e-6 at 390 eV, above the C K-edge, with rectangular markers indicating where image stacks were acquired between 380 eV and 575 eV, across the N K-edge, Ti L-edge, and O K-edge. Fig. 6b and c show the first and second principal component images, respectively, from the image stack over region R1. The PCA images from region R2 are not shown, though they are similar. Locales of high intensity in Fig. 6b and c correspond to the pixels that most closely match the respective PCA component spectra. Not surprisingly, the majority of the variance is explained by

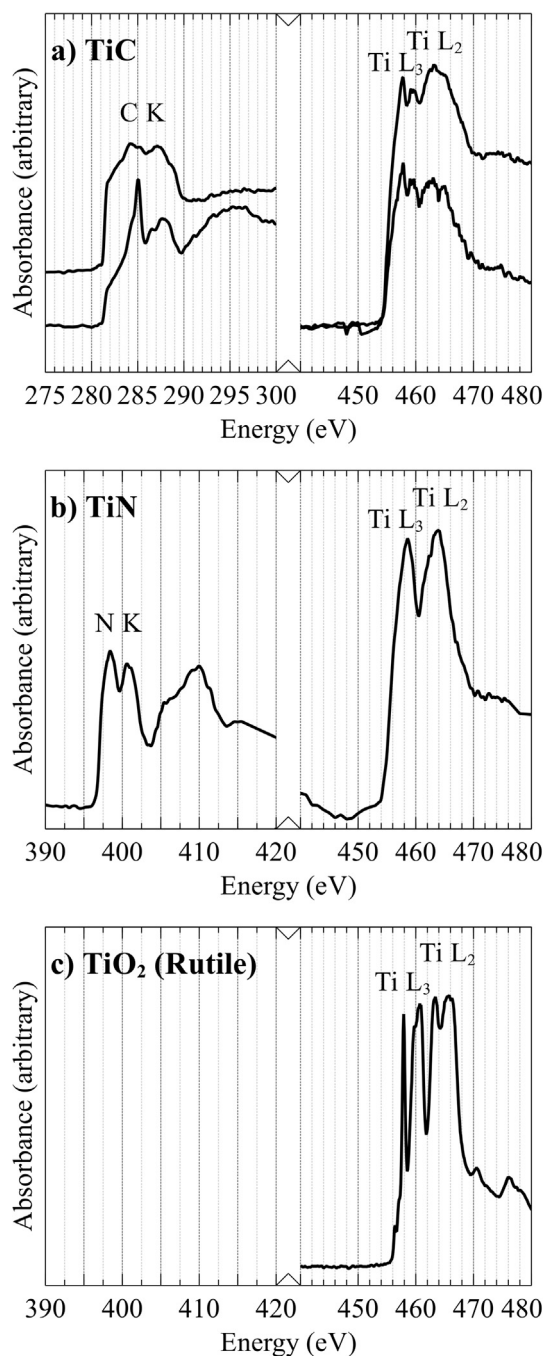


Fig. 5. Characteristic XANES spectra from (a) TiC and (b) TiN standards (this study) and (c) TiO<sub>2</sub> (rutile) from (Zega et al., 2012). TiC shows splitting in the Ti  $L_3$ -edge and minimal or no splitting in  $L_2$ . The C K-edge exhibits more variation than the Ti L-edge, varying between a sharp peak at 285 eV and a broader absorption at lower energy. The TiN K- and  $L_{3,2}$ -edges do not exhibit splitting. Rutile exhibits significant, well-defined splitting in both Ti-L edges.

the spectra from the graphitic regions (Fig. 6b), with voids where the Ti-rich subgrains comprise the next-most significant component, shown with high intensity in (Fig. 6c). PCA spectra from the graphite and each Ti-rich subgrain are shown in Fig. 6d. The graphite spectrum exhibits a

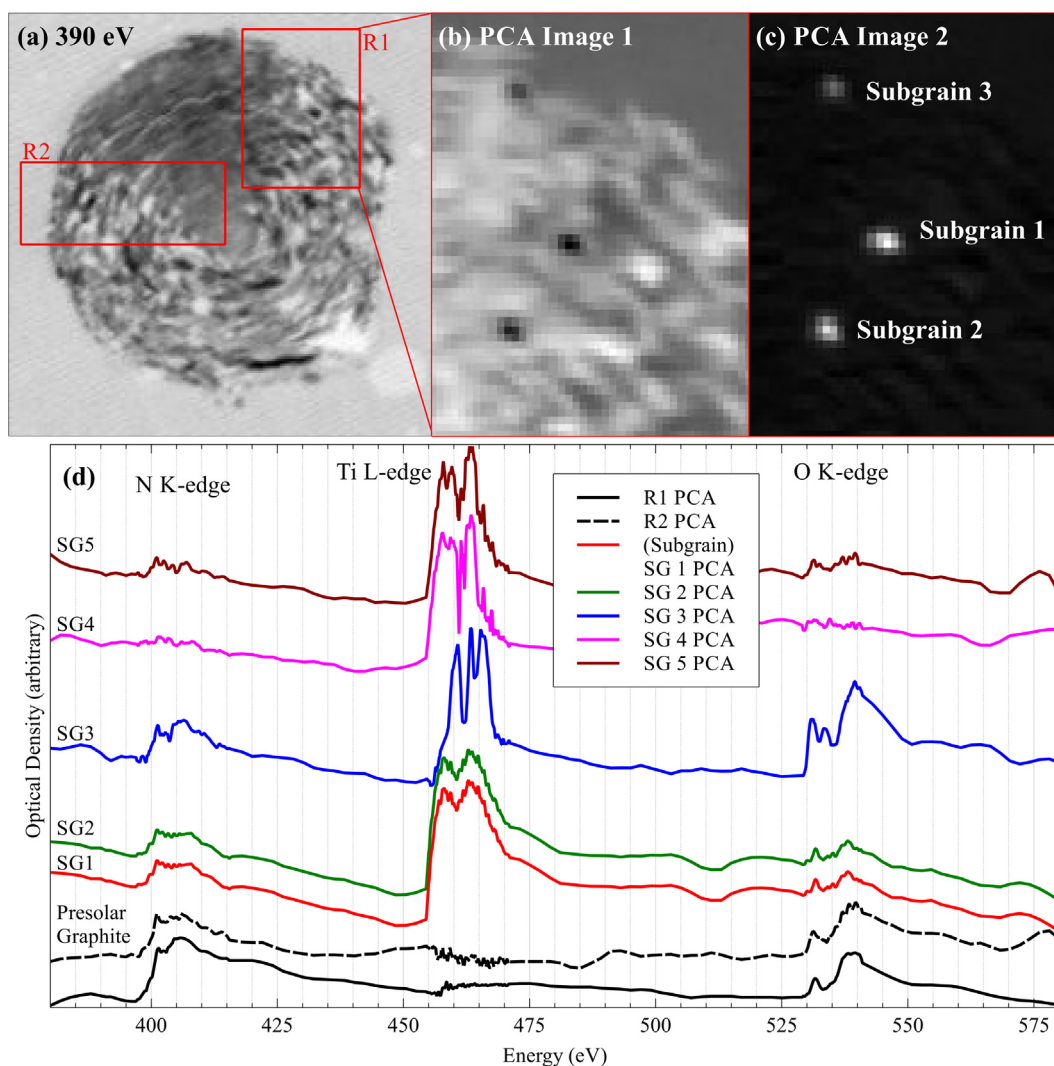


Fig. 6. STXM images and PCA spectra from presolar graphite grain KE3e-6. (a) Absorption contrast image at 390 eV, above the C K-edge. (b) First principal component image, accounting for the most spectral variance with major contributions from N and O K-edges. A relatively strong carboxyl peak near 532 eV is clearly present, matching the C K-edge spectrum from Fig. 3. (c) Second principal component with primary contribution from Ti L-edge. Three Ti-rich subgrains are apparent. (d) PCA spectra from graphite and Ti-subgrains with (b) PCA at the bottom and Subgrain 3 PCA at the top (color figure online). The Ti L-edges of Subgrains 1 and 2 match that of TiC or TiCN, while Subgrain 3 appears to be a rare rutile ( $\text{TiO}_2$ ) subgrain, though it lacks the lowest energy  $L_3$  absorption (see Fig. 5c). Subgrains may not extend fully through the microtome section, so some contribution from the graphite may be present in their spectra. (For interpretation of the references to colour in this figure legend, the reader is referred to the web version of this article.)

strong N absorbance, with a small peak near amidyl (401.9 eV) before the edge. It is difficult to confirm the presence of amidyl from the C K-edge spectrum (287.9–288.2 eV, Fig. 4a) due to its close proximity to the aliphatic and carboxyl absorbances. The spectrum shows a strong carboxyl absorbance at the O K-edge (532.0 eV), confirming the assignment from the C K-edge spectrum. A small enol absorbance is potentially present at 534.9 eV, but it is not possible to confirm its presence. The PCA spectra from both regions of the presolar graphite are similar.

Subgrains 1 and 2 (Fig. 6c,d) exhibit Ti L-edge absorbances matching those of TiC, the most common type of subgrain observed in presolar graphite by TEM, especially

those with SN origins (Croat et al., 2003). The shapes of the O and N K-edges differ from those of the surrounding graphite, which indicates the presence of N and O in the subgrain structure. This supports SIMS data showing increased ion yields of N and O from TiC subgrains, which are not completely due to matrix effects (Stadermann et al., 2005; Groopman et al., 2012a, 2014), and electron energy-loss spectroscopic (EELS) maps of TiC subgrains showing O and N concentrated in the occasionally present amorphous rims surrounding the carbides (Daulton et al., 2012). Approximately half of the TiC subgrains in KE3e6 have been observed to have 3–15 nm thick amorphous rims (Croat et al., 2003), which would not be resolved in the

STXM measurements. The spectrum for subgrain #3 most closely matches that of rutile (TiO<sub>2</sub>) (Brydson et al., 1989; Henderson et al., 2002; Zega et al., 2012), a rare subgrain type (Croat, 2007; Croat et al., 2008), with a significantly different Ti L-edge fine structure and much stronger O K-edge resonances. Interestingly, the Ti L-edge for absorption lacks a significant peak near 458 eV, where the lowest L<sub>3</sub> peak should be (compare with Fig. 5c). Rutile is highly oxidized and not generally expected to condense concurrently and under the same conditions as graphite and TiC in stellar ejecta. Subgrains 4 and 5 are likely TiC, as they do not show significant N or O K-edge absorptions, however their spectra are characterized by strong splitting of the L<sub>3</sub> peak and an L<sub>2</sub> band narrower than the standard TiC spectra. It is not known whether each subgrain extends through the entire microtome section, so the subgrain spectra likely contain contributions from the under/overlying graphite. This is especially apparent for the smallest subgrain, #3, whose N K-edge absorbance most closely matches that of the graphite spectrum. It is unlikely that there is much of a contribution to the N absorbance from TiO<sub>2</sub>, whereas TiC and TiN are isostructural.

KE3e6 was the only presolar grain in this study whose isotopic compositions was measured on the Cameca ims 3f. The isotopic data for this grain is limited, as only C, O, and Si isotopes were measured (Table 1). Among those, only C and O isotopes were anomalous, with <sup>12</sup>C/<sup>13</sup>C = 231, <sup>16</sup>O/<sup>18</sup>O = 290. These isotopes ratios are not diagnostic enough to unambiguously identify a stellar source, especially given the lack of significant <sup>28</sup>Si excesses, however, given its microstructural and subgrain content similarities to other SN graphite grains (Croat et al., 2003), which are distinctly different from those of presolar graphite grains with AGB origins (Croat et al., 2005) a SN origin remains the most likely.

### 3.3.2. OR1d5m-15

OR1d5m-15 appears to contain aliphatic and carboxyl resonances in its C K-edge spectra (Fig. 4a). Its N K-edge contains a small peak near amidyl (401.9 eV). The C K-edge spectrum also exhibits the pattern typical of graphite section damage, so the presence of amidyl and carboxyl resonances at the C K-edge are inconclusive. OR1d5m-15 is an LD graphite grain with <sup>12</sup>C/<sup>13</sup>C = 18.5, <sup>16</sup>O/<sup>18</sup>O = 408, <sup>14</sup>N/<sup>15</sup>N = 206, and a small depletion of <sup>28</sup>Si (Table 1). Aside from the C ratio, the isotopic anomalies are not large by presolar grain standards, though like most other LD graphite grains, a SN origin is the most likely.

### 3.3.3. OR1d5m-24

OR1d5m-24 has a complex complement of minor peaks between its graphitic π\* and σ\* excitons (Fig. 4a). These spectra are fairly noisy, but aliphatic, carboxyl, and probably carbonate resonances are identifiable. There is no shift in its π\* peak position. This grain has a <sup>12</sup>C/<sup>13</sup>C ratio of 318, <sup>16</sup>O/<sup>18</sup>O ratio of 306, <sup>14</sup>N/<sup>15</sup>N ratio of 229 (Table 1). Without measureable Si isotopic anomalies, a clear SN origin is not certain, though once more, like other LD graphite grains, this is most probable.

### 3.3.4. OR1d6m-5

OR1d6m-5 shows a strong aliphatic absorption and a π\* peak maximum at 285.3 eV (Fig. 4a). There are no TEM data for this grain. This grain exhibits the clear signatures of a SN origin: <sup>12</sup>C/<sup>13</sup>C = 45.9; <sup>16</sup>O/<sup>18</sup>O = 323; <sup>14</sup>N/<sup>15</sup>N = 248; δ<sup>29</sup>Si = -193‰; δ<sup>30</sup>Si = -308‰ (Table 1); δ<sup>25</sup>Mg = -43 ± 17‰; δ<sup>26</sup>Mg = 231 ± 20‰; initial <sup>26</sup>Al/<sup>27</sup>Al = 1.77 × 10<sup>-2</sup> (inferred from the excess of <sup>26</sup>Mg); and δ<sup>46,47,49,50</sup>Ti = 20 ± 11‰, 9 ± 12‰, 391 ± 18‰, 206 ± 82‰, respectively. Potassium and Ca isotopic ratios were not significantly different than terrestrial values.

### 3.3.5. OR1d6m-6

OR1d6m-6 is a unique and fascinating SN grain whose isotopic, chemical, and microstructural characteristics were discussed in detail in Groopman et al. (2014). In brief, this is the first reported LD presolar graphite grain containing a nanocrystalline core consisting of 3–4 nm sheets of graphene and surrounded by a mantle of turbostratic graphite (such grains are more common among high-density presolar graphite). C K-edge XANES of the core shows a nicely graphitic spectrum (Fig. 4a). Mantle spectra exhibit a carboxyl peak, potentially due to increased O content relative to the core or due to distorted interplanar bonding. The overall absorption in the mantle's plateau region is much higher relative to the π\* peak than that of the core spectra (see Fig. 4b). The π\* peak centers of mass are 285.2 eV for the core and 285.3 eV for the mantle.

This grain contains O and N isotopic heterogeneities (strong <sup>18</sup>O and <sup>15</sup>N enrichments) attributable both to internal subgrains and within the graphite structure itself, and a radial <sup>12</sup>C/<sup>13</sup>C gradient. The isotopic heterogeneities within the graphite structure cannot be linked directly to any microstructural differences. Numerous TiC, Fe-Ni, and SiC subgrains were identified in the TEM. Fig. 7 illustrates the size of the TiC subgrains vs. their atomic V/Ti ratios, quantified by energy dispersive X-ray spectroscopy (EDXS). These subgrains have a mean size of 162 ± 92 nm and a mean V/Ti ratio of 0.104 ± 0.010 (1σ), where the mean V/Ti ratio is weighted by the inverse square of the errors on the EDXS composition. These values are comparable to SN graphite grains in (Croat et al., 2003), where mean TiC subgrain sizes range from 30 nm to 232 nm and average V/Ti ratios range from 0.072 to 0.200. The SiC subgrain lies near the surface of OR1d6m-6 and consists of an intergrowth of 3C and 2H polytypes (not reported in Groopman et al. (2014)), though with a 3C lattice parameter of 4.77 Å, ~9.5% larger than the ideal value of 4.36 Å (Fig. 8). The convergent beam electron diffraction (CBED) pattern shows dark diffraction spots (solid red circles) that index to both the [112] zone of 3C-SiC and the [0001] zone of 2H-SiC. These diffraction spots are part of the {11-1} plane of 3C-SiC and the {10-10} plane of 2H-SiC. As in Hynes et al. (2010), the expected nominal 6% difference in d-spacings expected between these spots is not apparent. Spots indicated by dashed circles (blue circles) only index to the [0001] zone axis of 2H-SiC. This type of polymorph intergrowth has been previously observed in SiC X grains from SNe whose microstructures indicate that they formed under conditions

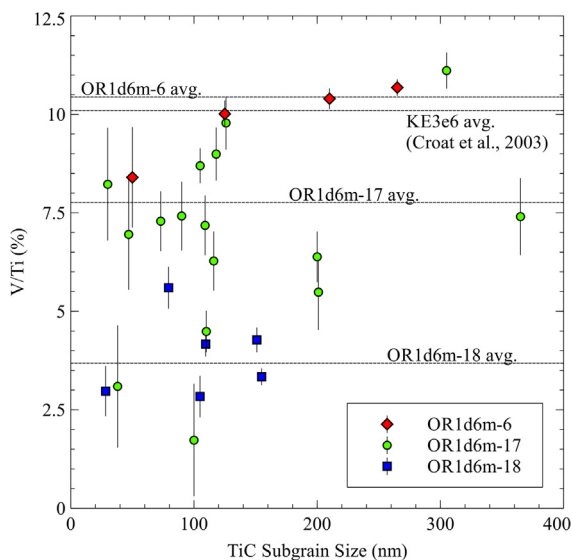


Fig. 7. Size vs. atomic V/Ti ratio determined by EDXS of TiC subgrains from presolar graphite grains OR1d6m-6,17,18. Averages for each graphite grain shown by dashed lines, weighted by the inverse square of the errors. There is no significant correlation between V/Ti ratio and subgrain size, though subgrains from each graphite grain tend to have similar V/Ti ratios.

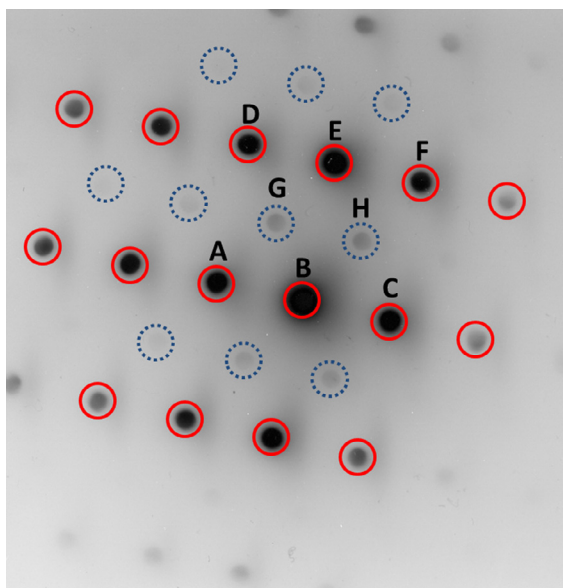


Fig. 8. Convergent beam electron diffraction (CBED) pattern from SiC subgrain within presolar graphite grain OR1d6m-6 showing an intergrowth between 3C-SiC and 2H-SiC polytypes. Dark diffraction spots (solid red circles) index to both the  $[11\bar{2}]$  zone of 3C-SiC and the  $[0001]$  zone of 2H-SiC. These diffraction spots are part of the  $\{11\bar{1}\}$  plane of 3C-SiC and the  $\{10\bar{1}0\}$  plane of 2H-SiC. As in Hynes et al. (2010), the expected nominal 6% difference in d-spacings expected between these spots is not apparent. Spots indicated by dashed circles (blue) only index to the  $[0001]$  zone axis of 2H-SiC. Letters above spots correspond to Miller Indices. A =  $(\bar{1}\bar{1}\bar{1})/(\bar{1}010)$ ; B =  $(000)/(0000)$ ; C =  $(11\bar{1})/(10\bar{1}0)$ ; D =  $(\bar{3}11)/(2200)$ ; E =  $(\bar{2}20)/(\bar{1}2\bar{1})$ ; F =  $(\bar{1}3\bar{1})/(0220)$ ; G =  $(\bar{1}100)$ ; H =  $(01\bar{1}0)$ . Adapted from Fig. 8 of (Hynes et al., 2010).

of high supersaturation and rapid growth (Hynes et al., 2010), which matches the conclusions of (Groopman et al., 2014). It should be noted that while OR1d6m-6 has one of the highest inferred initial  $^{26}\text{Al}/^{27}\text{Al}$  ratios measured in a presolar graphite grain (0.50) (Groopman et al., 2015), no  $^{44}\text{Ca}$  excesses indicative of extinct  $^{44}\text{Ti}$  was found in whole-grain measurements. This is potentially due to nearly all of the Ti being locked in TiC subgrains (Nittler et al., 1996) and not being sampled during those particular measurements. Further measurements of the Ti composition of the subgrains in microtome sections is necessary. The presence or lack of  $^{44}\text{Ti}$  in TiC subgrains could have a significant impact upon our understanding of dust formation and mixing in SN ejecta. Depth profile measurements of LD and HD SN graphite grains have shown a strong correlation between the ion intensities of  $^{44}\text{Ca}$  and  $^{48}\text{Ti}$ , and no correlation with  $^{40}\text{Ca}$ , when Ti-rich subgrains are inferred to be present in the profile (Zinner and Jadhav, 2013).

### 3.3.6. OR1d6m-8

OR1d6m-8 is one of the more singular presolar graphite grains from a XANES perspective. The  $\pi^*$  peak is broader than all other samples and appears to be split between two peaks at 285.1 and 285.5 eV (Fig. 4a). The center of mass was calculated as 285.45 eV. On the higher-energy side of the  $\pi^*$  peak lies a significant vinyl-keto absorption and a large aliphatic resonance. The background for this grain had to be treated differently from the other samples due to the wide  $\pi^*$  peak, which was not adequately fitted with a single Gaussian profile. Instead, the Gaussian was fixed to a center of 285.2 eV and its amplitude was set so that the residual in the minor peak region could not be negative. Fig. 4b shows a residual absorbance with strong splitting around the aromatic  $\pi^*$  peak, and very strong vinyl-keto and aliphatic absorptions. The relatively strong absorption between peaking near 288.9 eV could be due to urea. There are currently no TEM data for this grain.

Isotopically, OR1d6m-8 appears to be a fairly typical Type-II SN grain, though with a somewhat rare positive anomaly in  $^{29}\text{Si}$ :  $\delta^{29}\text{Si} = 88 \pm 29\%$ ,  $\delta^{30}\text{Si} = -120 \pm 31\%$  (Fig. 1, Table 1).  $^{12}\text{C}/^{13}\text{C} = 127.8$ ;  $^{16}\text{O}/^{18}\text{O} = 280$ ;  $^{14}\text{N}/^{15}\text{N} = 145$ ;  $\delta^{25}\text{Mg} = 2 \pm 12\%$ ;  $\delta^{26}\text{Mg} = 756 \pm 18\%$ ; inferred initial  $^{26}\text{Al}/^{27}\text{Al} = 7.71 \times 10^{-2}$ ;  $\delta^{42}\text{Ca} = 291 \pm 32\%$ ;  $\delta^{43}\text{Ca} = 719 \pm 81\%$ ;  $\delta^{44}\text{Ca} = 65 \pm 18\%$ ;  $\delta^{46}\text{Ti} = 31 \pm 11\%$ ;  $\delta^{47}\text{Ti} = -5 \pm 12\%$ ;  $\delta^{49}\text{Ti} = 1211 \pm 24\%$ ;  $\delta^{50}\text{Ti} = 801 \pm 106\%$ .

### 3.3.7. OR1d6m-13

OR1d6m-13 contains an aliphatic resonance and a  $\pi^*$  peak at 285.3 eV (Fig. 4a). This grain also contained a refractory metal nugget previously reported by (Croat et al., 2013), and though Mo XANES measurements were attempted, the subgrain was too small. Whole-grain NanoSIMS measurements yielded  $^{12}\text{C}/^{13}\text{C} = 66.0$ ;  $^{16}\text{O}/^{18}\text{O} = 170$ ;  $^{14}\text{N}/^{15}\text{N} = 263$ ;  $\delta^{29}\text{Si} = -289\%$ ;  $\delta^{30}\text{Si} = -337\%$  (Table 1);  $\delta^{25}\text{Mg} = 37 \pm 39\%$ ;  $\delta^{26}\text{Mg} = 11,666 \pm 217\%$ ; inferred initial  $^{26}\text{Al}/^{27}\text{Al} = 2.31 \times 10^{-1}$ ;  $\delta^{41}\text{K} = 1,146 \pm 58\%$ ;  $\delta^{42}\text{Ca} = 204 \pm 47\%$  (others normal);  $^{49}\text{Ti}/^{48}\text{Ti}$  was measured simultaneously with the Ca isotopes and was found to be normal

within errors, so the other Ti isotopes were not measured later. NanoSIMS images of ultramicrotomed thin sections show very strong gradients in the isotopic ratios of O and N (Fig. 9), and in the inferred  $^{26}\text{Al}/^{27}\text{Al}$  ratio (Fig. 10), similar to those observed in (Groopman et al., 2012a; Stadermann et al., 2005; Groopman et al., 2014). In the center of the grain,  $^{16}\text{O}/^{18}\text{O}$  ranges as low as 21, while  $^{14}\text{N}/^{15}\text{N}$  reaches 136, despite the whole-grain composition for N being terrestrial within errors. Total O and N counts are higher near the grain's outer edge than in the center where the isotopic anomalies are largest. This suggests the addition of terrestrial O and N, oxidation of the grain's outer layers, instead of an original gradient in the isotopic composition, although the grain's abundance of O-bearing functionalities appears low at the C K-edge relative to other graphite grains (Figs. 3 and 4). We also did not observe any heterogeneity in the XANES spectrum across the grain. Despite the isotopic gradients, the outer region remains isotopically anomalous, with  $^{16}\text{O}/^{18}\text{O} \sim 365 \pm 2$  and  $^{14}\text{N}/^{15}\text{N} \sim 265 \pm 2$ . OR1d6m-13 was a  $\sim 6 \mu\text{m}$  grain, so section B in Fig. 9 consists of material outside of the grain's center. Fig. 10 illustrates the first reported gradient in a presolar graphite for the inferred initial  $^{26}\text{Al}/^{27}\text{Al}$  ratio, which ranges up to 0.4 in a  $1.5 \mu\text{m}$  hotspot above the grain's center, nearly twice as high as the whole-grain measurement ( $^{26}\text{Al}/^{27}\text{Al} = 0.235$  in the whole microtome section). The

$^{26}\text{Mg}^+$  signal is much higher than, and not spatially correlated with,  $^{24}\text{Mg}^+$  or  $^{25}\text{Mg}^+$ . Section G in Fig. 10 is from close to the grain's center. The composition of OR1d6m-13 is consistent with a SN origin.

### 3.3.8. OR1d6m-17

OR1d6m-17 has a  $\pi^*$  peak at 285.3 eV (Fig. 4a) and a large aliphatic absorption. This grain's C, N, and O isotopic composition has been reported on in detail in (Groopman et al., 2012a), but also has a SN signature:  $^{12}\text{C}/^{13}\text{C} = 306.1$ ;  $^{16}\text{O}/^{18}\text{O} = 306$ ;  $^{14}\text{N}/^{15}\text{N} = 215$ ;  $\delta^{29}\text{Si} = -2\text{‰}$ ;  $\delta^{30}\text{Si} = -87\text{‰}$  (Table 1);  $\delta^{25}\text{Mg} = 119 \pm 28\text{‰}$ ;  $\delta^{26}\text{Mg} = 443 \pm 31\text{‰}$ ; inferred initial  $^{26}\text{Al}/^{27}\text{Al} = 5.58 \times 10^{-2}$ ;  $\delta^{49}\text{Ti} = 823 \pm 90\text{‰}$  (no other Ti anomalies);  $\delta^{42}\text{Ca} = 183 \pm 64\text{‰}$ ;  $\delta^{43}\text{Ca} = 381 \pm 150\text{‰}$ ;  $\delta^{44}\text{Ca} = 98 \pm 35\text{‰}$ . OR1d6m-17 is one of the few grains in this suite that exhibits a  $n$ -capture pattern in its Ca isotopes, though the Ca abundances are very low, hence the large error bars. Based upon the  $n$ -capture pattern, it is not possible to infer the initial presence of  $^{44}\text{Ti}$  from the abundance of  $^{44}\text{Ca}$ , though perhaps future NanoSIMS measurements of TEM thin sections will clarify this.

OR1d6m-17 contains numerous large TiC subgrains with sizes up to 365 nm (average =  $133 \pm 93$  nm) and a weighted mean V/Ti ratio of  $0.078 \pm 0.029$  (Fig. 7). The V/Ti ratios fall near the lower end of the range reported

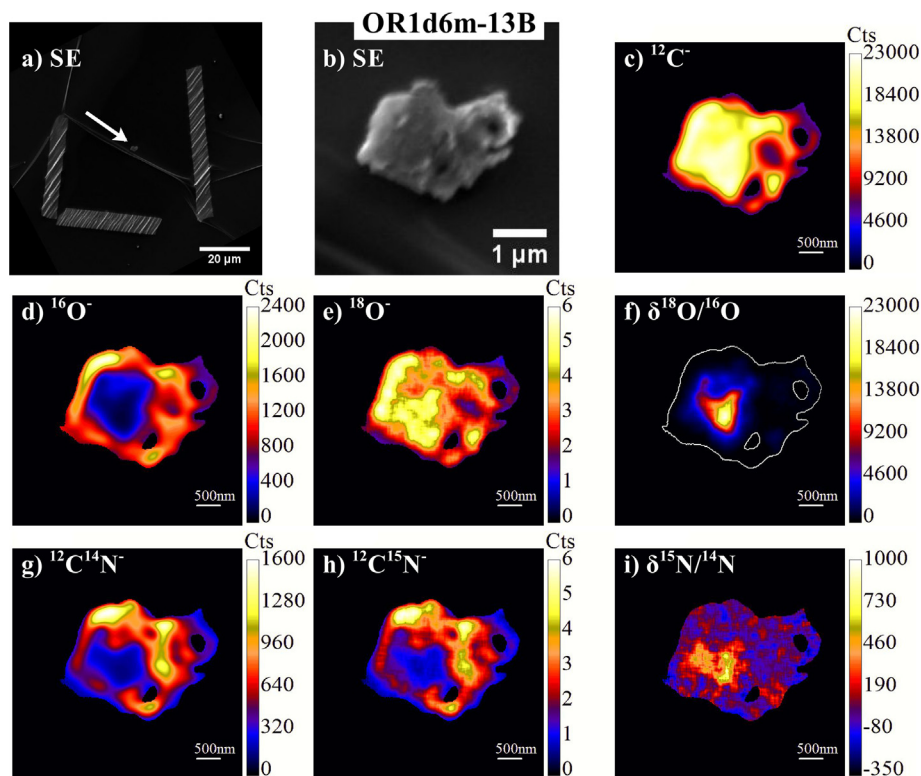


Fig. 9. NanoSIMS isotope ratio images of ultramicrotome section B of presolar graphite grain OR1d6m-13 on a Si wafer. All images are in the same orientation. Panels (a,b) show Auger Nanoprobe secondary electron (SE) images of section surrounded by carbon fibers. Panels (f,i) show gradients in  $\delta^{18}\text{O}/^{16}\text{O}$  and  $\delta^{15}\text{N}/^{14}\text{N}$ , up to 23,000‰ and 1,000‰, respectively ( $^{16}\text{O}/^{18}\text{O} \sim 21$ ;  $^{14}\text{N}/^{15}\text{N} \sim 136$ ). Total O and N contents are higher near the grain edge indicating that the grain was likely oxidized with terrestrial composition material, diluting the isotope anomalies. The magnitude of loss of original O and N cannot be determined. Panel (f) also shows an outline of the grain boundary for visual effect.

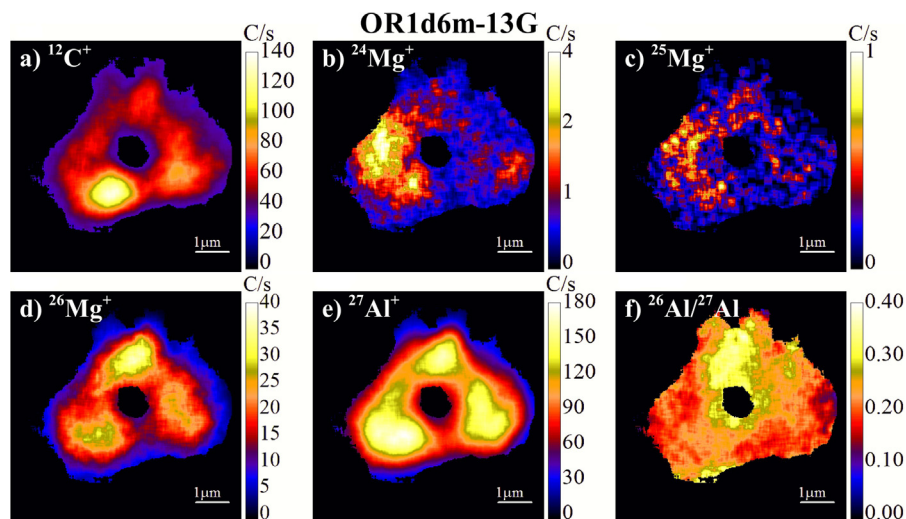


Fig. 10. NanoSIMS isotope images of ultramicrotomed section G of presolar graphite grain OR1d6m-13 on a Si wafer. Panels (a)–(e) show the average intensity across 15 frames; the hot spot in  $^{12}\text{C}^+$  (a) is the last region to sputter away, raising its average intensity.  $^{26}\text{Mg}^+$  (d) is much more intense than  $^{24}\text{Mg}^+$  (b), typical for SN grains, and correlates well with  $^{27}\text{Al}^+$  (e). The inferred initial  $^{26}\text{Al}/^{27}\text{Al}$  (f) is heterogeneous in this grain, however, peaking with a value of 0.4 in the  $\sim 1.5\ \mu\text{m}$  sized region above the hole (black) in the center of the microtome section.

in (Croat et al., 2003). Two Fe-Ni subgrains 50 nm and 40 nm in size were also found with Ni/Fe ratios of near  $0.063 \pm 0.004$ . The TiC subgrains were found to have strongly correlated excesses in  $^{18}\text{O}$  and  $^{15}\text{N}$  (Groopman et al., 2012a), indicative of material from the inner He/C zone of a SN (Rauscher et al., 2002; Bojazi and Meyer, 2014).

### 3.3.9. OR1d6m-18

OR1d6m-18 is one of the few grains with heterogeneous XANES spectra across multiple microtome sections. TEM and STXM images of OR1d6m-18 are shown in Fig. 11. One section has strong carboxyl and carbonate resonances, a small aliphatic absorption, and a  $\pi^*$  peak at 285.2 eV (Fig. 4a). Another section shows a stronger aliphatic resonance but lacks the other minor peaks and has a  $\pi^*$  peak at 285.45 eV. One section could be more heavily section-damaged than the other, resulting in stronger

carboxyl-region absorption. All of the TiC subgrains exhibit Ti L-edge spectra that closely match the TiC standard. The O K-edge XANES spectrum for the TiC subgrains is a rounded, featureless absorption. NanoSIMS isotope ratio images for C, N, and O are reported in (Groopman et al., 2012a). OR1d6m-18 has a SN signature:  $^{12}\text{C}/^{13}\text{C} = 121.0$ ;  $^{16}\text{O}/^{18}\text{O} = 149$ ;  $^{14}\text{N}/^{15}\text{N} = 433$ ;  $\delta^{29}\text{Si} = -29\text{‰}$ ;  $\delta^{30}\text{Si} = -12\text{‰}$  (Table 1);  $\delta^{25}\text{Mg} = -32 \pm 16\text{‰}$ ;  $\delta^{26}\text{Mg} = 259 \pm 18\text{‰}$ ; inferred initial  $^{26}\text{Al}/^{27}\text{Al} = 1.20 \times 10^{-2}$ ;  $\delta^{41}\text{K} = 283 \pm 45\text{‰}$ ;  $\delta^{42}\text{Ca} = 338 \pm 58\text{‰}$  (no other Ca anomalies);  $\delta^{49}\text{Ti} = 282 \pm 25\text{‰}$ ;  $\delta^{450}\text{Ti} = 506 \pm 124\text{‰}$  (no  $^{46}\text{Ti}$  or  $^{47}\text{Ti}$  anomalies).

OR1d6m-18 contains TiC subgrains with an average size of  $105 \pm 47\ \text{nm}$  and a weighted mean V/Ti ratio of  $0.037 \pm 0.010$  (Fig. 7). As shown in Fig. 11, the TiC subgrains are concentrated near the graphite grain's center. The V/Ti ratios of the TiC subgrains are substantially lower than those in most other SN graphite grains, potentially

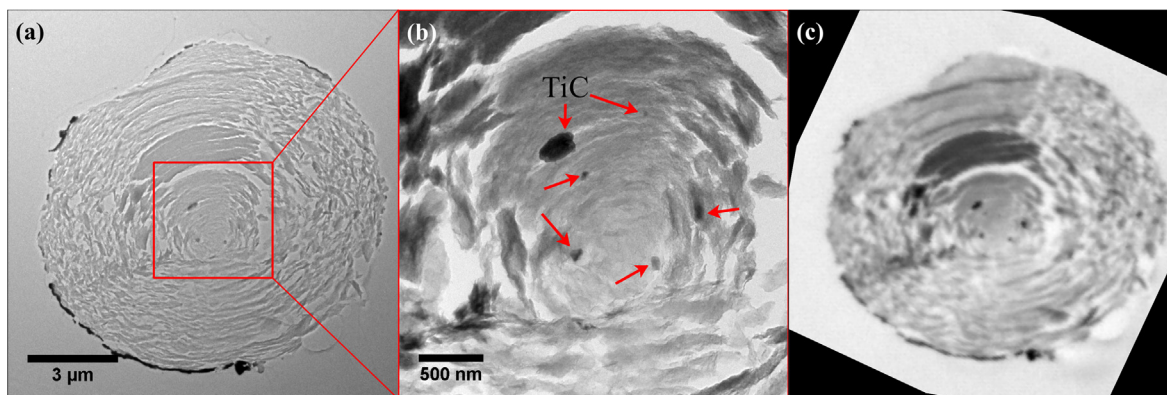


Fig. 11. (a–b) TEM micrographs and (c) STXM X-ray absorption image at 464 eV of presolar grain OR1d6m-18 section. TiC subgrains are darkly contrasting spots indicated by arrows (b). Ring of dark contrast in (a) is redeposited Au from the original substrate used for NanoSIMS measurements (b) is inset of (a).

indicating a higher temperature formation environment as VC is less refractory than TiC (Lodders and Fegely, 1995; Croat et al., 2003). Of particular interest is the presence of Ca in three TiC subgrains, up to  $3 \pm 0.4$  atomic% (quantifying only Ti, V, and Ca), with Ca/Ti ratios of  $(9.49 \pm 1.05) \times 10^{-3}$ ,  $(21.01 \pm 2.12) \times 10^{-3}$ , and  $(31.85 \pm 4.28) \times 10^{-3}$ . The background Ca signal from the surrounding graphite grain and from the instrument is zero to the limit of detector sensitivity. The observed Ca is thus most likely radiogenic  $^{44}\text{Ca}$  intrinsic to the TiC subgrains from the decay of  $^{44}\text{Ti}$ . The measured Ca/Ti ratios would indicate initial  $^{44}\text{Ti}/^{48}\text{Ti}$  ratios up to  $\sim 4.3 \times 10^{-2}$ , comparable to values previously seen in presolar supernova SiC and graphite grains (Nittler et al., 1996; Lin et al., 2010). Given the similarity of V/Ti ratios in the subgrains and the close spatial proximity near the graphite grain's center, we wonder why Ca is only detectable in three of the six TiC subgrains, though perhaps this is only a function of detector sensitivity. Future NanoSIMS measurements should be able to clarify these results. Vastly different inferred initial  $^{44}\text{Ti}/^{48}\text{Ti}$  ratios within the TiC subgrains will provide substantial information regarding the role of mixing and the degree of isotopic heterogeneity within SN ejecta. The striking correlation between  $^{18}\text{O}$  and  $^{15}\text{N}$  excesses in TiC subgrains from OR1d6m-18 and other SN graphite grains (Groopman et al., 2012a; Groopman et al., 2014) provides strong evidence that this material originated from the inner He/C zone (Rauscher et al., 2002; Bojazi and Meyer, 2014). Titanium-44, however, forms in the Fe/Ni cores and Si-rich zones of SNe (Woosley and Weaver, 1995; Rauscher et al., 2002), so this Ti must be mixed with material from the outer layers prior to grain condensation.

### 3.3.10. OR1d6m-23

OR1d6m-23's C K-edge spectra contains distinct vinyl-keto and carboxyl resonances and a much shallower slope approaching the  $\sigma^*$  excitons, potentially indicative of a carbonate absorption (Fig. 4a). This feature stands out strongly at  $\sim 288.7$  eV in Fig. 4b. The  $\pi^*$  peak lies at 285.1 eV. OR1d6m-23 shows strong evidence for a SN origin:  $^{12}\text{C}/^{13}\text{C} = 73.7$ ;  $^{16}\text{O}/^{18}\text{O} = 394$ ;  $^{14}\text{N}/^{15}\text{N} = 214$ ;  $\delta^{29}\text{Si} = -281\text{‰}$ ;  $\delta^{30}\text{Si} = -398\text{‰}$  (Table 1);  $\delta^{25}\text{Mg} = 19 \pm 15\text{‰}$ ;  $\delta^{26}\text{Mg} = 1,509 \pm 28\text{‰}$ ; inferred initial  $^{26}\text{Al}/^{27}\text{Al} = 0.13$ . It also shows  $\delta^{49}\text{Ti}/^{48}\text{Ti} = 242 \pm 39\text{‰}$ ,  $\delta^{50}\text{Ti}/^{48}\text{Ti} = 660 \pm 197\text{‰}$ , and no discernable  $^{46,47}\text{Ti}$  or Ca isotope anomalies. There is a disparity between the very strong evidence for a SN origin but a lack of evidence for extinct  $^{44}\text{Ti}$ , especially in light of the strong  $^{28}\text{Si}$  enrichment in this grain. For example, many SN SiC-X grains with similar Si, C, and Al isotopic compositions to OR1d6m-23 show evidence for extinct  $^{44}\text{Ti}$  since  $^{28}\text{Si}$  and  $^{44}\text{Ti}$  are co-produced in the same inner SN zone (Nittler et al., 1996; Lin et al., 2010).

### 3.3.11. OR1d6m-24

OR1d6m-24 contains an apparent carboxyl absorption, which is also visible at the O K-edge (Fig. 4a). Its  $\pi^*$  peak center is at the canonical 285.2 eV position. One large ( $\sim 300$  nm) TiC subgrain is located near the graphite grain's center. Its Ti L-edge XANES matches that of the TiC

standard. OR1d6m-24, heavily enriched in  $^{13}\text{C}$ , was reported to have a radial C isotope ratio gradient (Groopman et al., 2012a). The origins of OR1d6m-24 are difficult to determine as it contains essentially no isotopic anomalies in N, O, Si, Mg, Ca, or Ti.  $\delta^{50}\text{Ti}/^{48}\text{Ti}$  is potentially anomalous on the order of  $8000 \pm 1000\text{‰}$ , however nearly 80% of the measured mass 50 ion signal was due to the  $^{50}\text{Cr}$  isobar, inferred from monitoring  $^{52}\text{Cr}$  during the measurement. Surface Cr contamination is a byproduct of the dichromate treatment used during acid separation from the meteorite host rock (Amari et al., 1994). Given this large correction and the lack of other significant anomalies other than C, the  $^{50}\text{Ti}$  anomaly must be met with caution. The microstructure, subgrain content, and V/Ti composition of its TiC subgrains exhibit similarities to SN graphite grains. The lack of minor-element anomalies in this grain might be indicative of isotope dilution, though Groopman et al. (2012a) concluded that the radial isotope gradient in  $^{12}\text{C}/^{13}\text{C}$  is more likely due to changes in the isotopic composition of the stellar environment during condensation.

### 3.3.12. OR1g2m-4

OR1g2m-4 was the only HD graphite grain in our XANES study, though its internal crystal structure resembles turbostratic graphite more than "onion"-like HD grains. All spectra show a strong carboxyl peak near the C K-edge; occasional spectra indicate the minor presence of vinyl-keto groups (Fig. 4a). The  $\pi^*$  peak lies at 285.2 eV. HD graphite grains typically do not contain O or N isotopic anomalies, so neither of these elements were measured for the OR1g2m suite of grains. C, Si, K, Ca, and Ti were all measured with the NanoSIMS. While this grain did not contain any anomalies in K, Ca,  $^{47,50}\text{Ti}$ , or  $^{30}\text{Si}$ , it had  $^{12}\text{C}/^{13}\text{C} = 77.8 \pm 0.3$ ,  $\delta^{29}\text{Si}/^{28}\text{Si} = -67 \pm 28\text{‰}$ ,  $\delta^{46}\text{Ti}/^{48}\text{Ti} = 243 \pm 66\text{‰}$ , and  $\delta^{49}\text{Ti}/^{48}\text{Ti} = 2230 \pm 90\text{‰}$ . Based upon these isotopes alone, a progenitor is difficult to identify, though a SN origin is possible.

## 4. DISCUSSION AND CONCLUSION

We have observed a wide variety of XANES spectra from presolar graphite grains, most or all of which originated in the ejecta of Type-II supernovae, with significant variability in the non-aromatic minor peaks near the C K-edge. Despite the difficulty in distinguishing some of these minor peaks from microtome-induced damage to the graphite structure, we have observed an anti-correlation between the presence of vinyl-keto and aliphatic peaks, and a correlation between carboxyl and carbonate resonances. It remains unknown whether turbostratic graphite intrinsically exhibits absorption features near 288.4 eV that mimic "section damage" due to its increased layer spacing and smaller domain size than ideal graphite (Croat et al., 2003; Groopman et al., 2014). XANES spectra were found to be uniform across individual microtome sections (discounting polarization and orientation effects), even in grains with strong isotope ratio heterogeneities in C, N, and O. This also appears to discount the potential intrusion of LR White resin into the presolar grain

structure where it could mask intrinsic resonances in the amide, carbonate, and carboxyl regions. While heterogeneous contamination from LR White resin appears unlikely, we cannot rule out migration of resinous material over the surfaces of the microtome sections during electron and X-ray beam analyses or from ultramicrotomy. Such homogeneous contamination over the microtome sections would dilute subsequently measured isotope ratios. The only example of XANES heterogeneity observed in a single grain is from OR1d6m-18 in spectra from two different microtome sections. These particular spectral differences, however, cannot be differentiated from possible section damage.

We have also observed the first reported radial gradient in the inferred initial  $^{26}\text{Al}/^{27}\text{Al}$  ratio within a presolar graphite grain, adding Al to the above list of potentially heterogeneous elements within the graphite structure. Isotopic heterogeneities in  $^{26}\text{Al}/^{27}\text{Al}$  have also been observed in a SiC X grain. Isotope ratio gradients have been attributed both to effects during condensation (e.g., ejecta mixing and/or granular transport) and to isotope dilution effects (e.g., mixing with isotopically normal material in the early Solar System, host meteorite or laboratory), especially in the HD presolar graphite grains (Hoppe et al., 1995; Zinner et al., 1995; Stadermann et al., 2005; Groopman et al., 2014). This outstanding issue is of significant importance to the interpretation of presolar grain formation and evolution. It remains unknown to what degree isotope dilution may affect the local chemistry of the sample. Are certain bonding environments more susceptible to isotope dilution? The lack of XANES heterogeneity within individual samples suggests that this is not the case, or that the relative proportions of different environments is not near enough to parity for these effects to be visible. Of particular interest and concern are *in-situ* studies of insoluble organic material from the Murchison CM2 carbonaceous chondrite, whose C K-edge spectra were shown to be altered by HF-HCl treatments similar to those used to extract the presolar graphite grains (Flynn et al., 2010; Yabuta et al., 2010). It remains unknown to what extent graphitic and turbostratic materials are affected by these treatments.

We suggest that similar NanoSIMS and XANES studies of presolar SiC grains should be undertaken, both because SiC is the most-studied presolar mineral type and since it is expected to be less susceptible to isotope dilution effects than presolar graphite. We also plan to further analyze the thin sections in this study using NanoSIMS to identify elemental and isotopic heterogeneities. These studies may help constrain the proportion of isotopic heterogeneities attributable to primary versus secondary processes. We have also observed detectable levels of Ca by EDXS in TiC subgrains in presolar graphite grain OR1d6m-18, which indicates the potential initial presence of  $^{44}\text{Ti}$  up to ~4% relative to  $^{48}\text{Ti}$ . Future NanoSIMS measurements will be able to confirm this. Correlated  $^{18}\text{O}$  and  $^{15}\text{N}$  excesses in these subgrains (Groopman et al., 2012a) indicate an inner He/C zone origin for TiC material (Rauscher et al., 2002; Bojazi and Meyer, 2014), however the presence of  $^{44}\text{Ti}$ , which is synthesized in the Fe-Ni core and Si-rich surrounding layers (Woosley and Weaver, 1995; Rauscher et al.,

2002), implies that significant mixing in the stellar ejecta is required prior to grain condensation. The presence of V in TiC subgrains up to ~10 at.% relative to Ti likely affects the Ti L-edge and C K-edge XANES spectra, though the quality of these spectra were not sufficient to tease out such details. NanoSIMS measurements of O isotopes in the rutile-like subgrain in KE3e6 would also be indicative of whether post-formation processing had a significant effect, e.g., terrestrial O isotopes would point to a Ti-rich subgrain such as TiC having been completely oxidized following the condensation of the graphite grain. It would therefore be impossible to rule out alternation of the host graphite grain as well. Additionally, O-rich subgrains within presolar graphite are more ideal samples than TiC, since the C isotopic composition of the latter is quite difficult to differentiate from the host graphite grain, so this measurement would be unambiguous. It should be emphasized, however, that even though the precise effects and magnitude of post-formation processing remain unknown in presolar graphite grains, all of the grains from Orgueil have experienced the same history within the host meteorite and in the laboratory during and after separation. Therefore, the variety of observed XANES spectra must be, at least in part, primary formation features.

A considerable variety of polycyclic aromatic hydrocarbon (PAH) and aliphatic molecules have been observed by their infrared (IR) emission around a variety of AGB stars and within the interstellar medium (e.g., (Draine, 2003; Salama, 2008) and references therein). These are most likely the leftover precursor material from which some micron-sized graphite grains condensed in the stellar ejecta. Given the complexity of the C K-edge XANES spectra and relatively simple models used for fitting, we could not yet quantify the relative abundance of different C molecules within the presolar graphite grains. These observations would be of great utility in helping constrain the abundance of such molecules in planetary nebulae. O content has been shown to increase with the level of disorder in presolar graphite grains (Croat et al., 2008), so modeling the effects of O content and aliphatic abundance in poor-to-well-crystallized graphite on C K-edge XANES would be most useful.

XANES has the potential to sensitively probe chemical heterogeneities in the compositions of presolar grains due to isotopic dilution from secondary processing and to quantify the abundance of chemical functionalities. HD graphite grains, which are inferred to be more susceptible to isotopic dilution than LD grains, should be investigated in more depth. The wide variety of structure at the C K-edge implies heterogeneous formation environments and/or varying degrees of post-formation alteration. Given the outstanding and important nature of problems such as isotopic dilution, secondary processing, and their effects upon our inferences of stellar environments, such as the abundances of different molecule types, XANES could have a significant role to play in future presolar grain investigations. Spectral modeling based upon the variety of XANES observations here will aid in the quantification of molecular species. XANES has so far proven to provide complementary, non-destructive chemical information to correlated TEM and NanoSIMS studies.

## ACKNOWLEDGEMENTS

The authors would like to thank A. L. David Kilcoyne for help with the STXM at beamline 5.3.2.2; Tom Bernatowicz for ultramicrotome work; Rhonda Stroud and George Cody for sharing beamline time; Jill Pasteris for providing a sample of Ceylon graphite; Kevin Croat and Sachiko Amari for providing presolar graphite grain KE3e-6 and the former for TEM work on grain OR1d6m-24; and Jay Brandes for sharing data from his 2008 paper for comparison. We would like to thank the reviewers for their helpful suggestions. This work was supported by NASA Earth and Space Science Fellowship (NESSF) NNX11AN60H (EEG) and NASA grant NNX10AI63G (LRN). This research was performed while the author held an NRC Research Associateship award at the U.S. Naval Research Laboratory (EEG). The Advanced Light Source is supported by the Director, Office of Science, Office of Basic Energy Sciences, of the U.S. Department of Energy under Contract No. DE-AC02-05CH11231.

## REFERENCES

- Ahuja R., Bruhwiler P. A., Wills J. M., Johansson B., Martensson N. and Eriksson O. (1996) Theoretical and experimental study of the graphite 1s X-ray absorption edges. *Phys. Rev. B: Condens. Matter* **54**, 14396–14404.
- Amari S., Anders E., Virag A. and Zinner E. (1990) Interstellar graphite in meteorites. *Nature* **345**, 238–240.
- Amari S., Lewis R. S. and Anders E. (1994) Interstellar grains in meteorites: I. Isolation of SiC, graphite and diamond; size distributions of SiC and graphite. *Geochim. Cosmochim. Acta* **58**, 459–470.
- Amari S., Zinner E. and Lewis R. S. (1995) Large  $^{18}\text{O}$  excesses in circumstellar graphite grains from the Murchison meteorite: indication of a massive-star origin. *Astrophys. J.* **447**, L147–L150.
- Belavin V. V., Okotrub A. V., Bulusheva L. G., Kotosonov A. S., Vyalykh D. V. and Molodtsov S. L. (2006) Determining misorientation of graphite grains from the angular dependence of X-ray emission spectra. *J. Exp. Theor. Phys.* **103**, 604–610.
- Benfatto M. and Della Longa S. (2001) Geometrical fitting of experimental XANES spectra by a full multiple-scattering procedure. *J. Synchrotron Radiat.* **8**, 1087–1094.
- Bernatowicz T., Fraundorf G., Ming T., Anders E., Wopenka B., Zinner E. and Fraundorf P. (1987) Evidence for interstellar SiC in the Murray carbonaceous meteorite. *Nature* **330**, 728–730.
- Bernatowicz T. J., Cowsik R., Gibbons P. C., Lodders, Jr., K. B. F., Amari S. and Lewis R. S. (1996) Constraints on stellar grain formation from presolar graphite in the Murchison meteorite. *Astrophys. J.* **472**, 760–782.
- Bojazi M. and Meyer B. (2014) Explosive nucleosynthesis of  $^{15}\text{N}$  in a massive star model. *Phys. Rev. C: Nucl. Phys.* **89**, 025807, 1–19.
- Brandes J. A., Cody G. D., Rumble D., Haberstroh P., Wirick S. and Gelinis Y. (2008) Carbon K-edge XANES spectromicroscopy of natural graphite. *Carbon* **46**, 1424–1434.
- Bruhwiler P. A., Maxwell A. J., Puglia C., Nilsson A., Anderson S. and Martensson N. (1995) Pi-asterisk and sigma-asterisk excitons in C-1s absorption of graphite. *Phys. Rev. Lett.* **74**, 614–617.
- Brydson R., Sauer H., Engel W., Thomass J. M., Zeitler E., Kosugi N. and Kuroda H. (1989) Electron energy loss and X-ray absorption spectroscopy of rutile and anatase: a test of structural sensitivity. *J. Phys.: Condens. Matter* **1**, 797–812.
- Campagnola L. (2016) PyQTGraph: Scientific Graphics and GUI Library for Python.
- Cody G. D., Botto R. E., Ade H., Behal S., Disko M. and Wirick S. (1995) Inner-shell spectroscopy and imaging of a subbituminous coal: in-situ analysis of organic and inorganic microstructure using C(1s)-, Ca(2p)-, and Cl(2s)-NEXAFS. *Energy Fuels* **9**, 525–533.
- Cody G. D., Ade H., Alexander C. M. O'D., Araki T., Butterworth A., Fleckenstein H., Flynn G., Gilles M. K., Jacobsen C., Kilcoyne A. L. D., Messenger K., Sandford S. A., Tyliczszak T., Westphal A. J., Wirick S. and Yabuta H. (2008) Quantitative organic and light-element analysis of comet 81P/Wild 2 particles using C-, N-, and O- $\mu$ -XANES. *Meteorit. Planet. Sci.* **43**, 353–365.
- Cristallo S., Piersanti L., Straniero O., Gallino R., Domínguez I., Abia C., Di Rico G., Quintini M. and Bisterzo S. (2011) Evolution, nucleosynthesis, and yields of low-mass asymptotic giant branch stars at different metallicities. II. The FRUITY Database. *Astrophys. J. Suppl. S.* **197**, 17.
- Croat T. K. (2007) Rutile found within presolar graphites from Murchison, 70th Annual Meteoritical Society Meeting. *Meteorit. Planet. Sci.*, Tucson, #5217(abstr.).
- Croat T. K., Bernatowicz T., Amari S., Messenger S. and Stadermann F. J. (2003) Structural, chemical, and isotopic microanalytical investigations of graphite from supernovae. *Geochim. Cosmochim. Acta* **67**, 4705–4725.
- Croat T. K., Stadermann F. J. and Bernatowicz T. J. (2005) Presolar graphite from AGB stars: microstructure and s-process enrichment. *Astrophys. J.* **631**, 976–987.
- Croat T. K., Stadermann F. J. and Bernatowicz T. J. (2008) Correlated isotopic and microstructural studies of turbostratic presolar graphite from the Murchison meteorite. *Meteorit. Planet. Sci.* **43**, 1497–1516.
- Croat T. K., Berg T., Bernatowicz T., Groopman E. and Jadhav M. (2013) Refractory metal nuggets within presolar graphite: first condensates from a circumstellar environment. *Meteorit. Planet. Sci.* **48**, 686–699.
- Daulton T. L., Eisenhour D. D., Bernatowicz T. J., Lewis R. S. and Buseck P. R. (1996) Genesis of presolar diamonds: comparative high-resolution transmission electron microscopy study of meteoritic and terrestrial nano-diamonds. *Geochim. Cosmochim. Acta* **60**, 4853–4872.
- Daulton T. L., Bernatowicz T. J. and Croat T. K. (2012) Electron energy loss spectral imaging of TiC formed by Supernovae: a scanning transmission electron microscopy study of grain formation and alteration mechanisms. 43rd Lunar and Planetary Science Conference. Lunar and Planetary Institute, Houston, p. #2247(abstr.).
- De Gregorio B. T., Stroud R. M., Nittler L. R., Alexander C. M. O'D., Kilcoyne A. L. D. and Zega T. J. (2010) Isotopic anomalies in organic nanoglobules from Comet 81P/Wild 2: comparison to Murchison nanoglobules and isotopic anomalies induced in terrestrial organics by electron irradiation. *Geochim. Cosmochim. Acta* **74**, 4454–4470.
- De Gregorio B. T., Stroud R. M., Cody G. D., Nittler L. R., David Kilcoyne A. L. and Wirick S. (2011) Correlated microanalysis of cometary organic grains returned by Stardust. *Meteorit. Planet. Sci.* **46**, 1376–1396.
- De Gregorio B. T., Stroud R. M., Nittler L. R., Alexander C. M. O. D., Bassim N. D., Cody G. D., Kilcoyne A. L. D., Sandford S. A., Milam S. N., Nuevo M. and Zega T. J. (2013) Isotopic and chemical variation of organic nanoglobules in primitive meteorites. *Meteorit. Planet. Sci.* **48**, 904–928.
- Draine B. T. (2003) Interstellar dust grains. *Annu. Rev. Astron. Astrophys.* **41**, 241–289.
- Fedkin A. V., Meyer B. S. and Grossman L. (2010) Condensation and mixing in supernova ejecta. *Geochim. Cosmochim. Acta* **74**, 3642–3658.

- Feuerstein D., Parker K. H. and Boutelle M. G. (2009) Practical methods for noise removal: applications to spikes, nonstationary quasi-periodic noise, and baseline drift. *Anal. Chem.* **81**, 4987–4994.
- Fischer D. A., Wentzcovitch R. M., Carr R. G., Continenza A. and Freeman A. J. (1991) Graphitic interlayer states: a carbon K near-edge X-ray-absorption fine-structure study. *Phys. Rev. B: Condens. Matter* **44**, 1427–1429.
- Flynn G. J., Keller L. P., Wirick S., Jacobsen C. and Sutton S. R. (2003) Analysis of interplanetary dust particles by soft and hard X-ray microscopy. *Journal de Physique IV (Proceedings)* **104**, 367–372.
- Flynn G. J., Wirick S., Keller L. P. and Jacobsen C. (2010) Modification of the Murchison insoluble organic matter (IOM) by acid extraction. Astrobiology Science Conference 2010: Evolution and Life: Surviving Catastrophes and Extremes on Earth and Beyond, League City, LPI Contribution No. 1538, p.5162(abstr.).
- Flynn G. J., Wirick S. and Keller L. P. (2013) Organic grain coatings in primitive interplanetary dust particles: implications for grain sticking in the Solar Nebula. *Earth Planets Space* **65**, 1159–1166.
- Francis J. T. and Hitchcock A. P. (1992) Inner-shell spectroscopy of p-benzoquinone, hydroquinone, and phenol: distinguishing quinoid and benzenoid structures. *J. Phys. Chem. C* **96**, 6598–6610.
- Gallino R., Raiteri C. M., Busso M. and Matteucci F. (1994) The puzzle of silicon, titanium, and magnesium anomalies in meteoritic silicon carbide grains. *Astrophys. J.* **430**, 858.
- Groopman E., Bernatowicz T. and Zinner E. (2012a) C, N, and O isotopic heterogeneities in low-density supernova graphite grains from Orgueil. *Astrophys. J. Lett.* **754**, L8.
- Groopman E. E., Daulton T. L., Nittler L. R., Bernatowicz T. J. and Zinner E. K. (2012b) Ti-XANES and EELS of presolar TiC subgrains within low-density supernova graphite grains, 75th Annual Meteoritical Society Meeting. *Meteorit. Planet. Sci.* Cairns, AU, p. #5225(abstr.).
- Groopman E., Nittler L. R., Bernatowicz T. and Zinner E. (2014) NanoSIMS, TEM, and XANES studies of a unique presolar supernova graphite grain. *Astrophys. J.* **790**, 9–22.
- Groopman E., Zinner E., Amari S., Gyngard F., Hoppe P., Jadhav M., Lin Y., Xu Y., Marhas K. and Nittler L. R. (2015) Inferred initial  $^{26}\text{Al}/^{27}\text{Al}$  ratios in presolar stardust grains from supernovae are higher than previously estimated. *Astrophys. J.* **809**, 31.
- Henderson G. S., Liu X. and Fleet M. E. (2002) A Ti L-edge X-ray absorption study of Ti-silicate glasses. *Phys. Chem. Miner.* **29**, 32–42.
- Herd C. D., Blinova A., Simkus D. N., Huang Y., Tarozo R., Alexander C. M. O'D., Gyngard F., Nittler L. R., Cody G. D., Fogel M. L., Kebukawa Y., Kilcoyne A. L., Hilts R. W., Slater G. F., Glavin D. P., Dworkin J. P., Callahan M. P., Elsila J. E., De Gregorio B. T. and Stroud R. M. (2011) Origin and evolution of prebiotic organic matter as inferred from the Tagish Lake meteorite. *Science* **332**, 1304–1307.
- Hitchcock A.P. (1997–2016) aXis 2000 – Analysis of X-ray Images and Spectra. McMaster University.
- Hoppe P., Amari S., Zinner E. and Lewis R. S. (1995) Isotopic compositions of C, N, O, Mg, and Si, trace element abundances, and morphologies of single circumstellar graphite grains in four density fractions from the Murchison meteorite. *Geochim. Cosmochim. Acta* **59**, 4029–4056.
- Hutcheon I. D., Huss G. R., Fahey A. J. and Wasserburg G. J. (1994) Extreme Mg-26 and O-17 enrichments in an Orgueil corundum: identification of a presolar oxide grain. *Astrophys. J. Lett.* **425**, L97–L100.
- Hynes K. M., Croat T. K., Amari S., Mertz A. F. and Bernatowicz T. J. (2010) Structural and isotopic microanalysis of presolar SiC from supernovae. *Meteorit. Planet. Sci.* **45**, 596–614.
- Jadhav M., Amari S., Zinner E. and Maruoka T. (2006) Isotopic analysis of presolar graphite grains from Orgueil. *New Astron. Rev.* **50**, 591–595.
- Jadhav M., Zinner E., Amari S., Maruoka T., Marhas K. K. and Gallino R. (2013) Multi-element isotopic analyses of presolar graphite grains from Orgueil. *Geochim. Cosmochim. Acta* **113**, 193–224.
- Jones E., Oliphant T., Peterson P. et al. (2001) SciPy: Open Source Scientific Tools for Python.
- Karunakaran C., Christensen C. R., Gaillard C., Lahli R., Blair L. M., Perumal V., Miller S. S. and Hitchcock A. P. (2015) Introduction of soft X-Ray spectromicroscopy as an advanced technique for plant biopolymers research. *PLoS ONE* **10**(3), e0122959.
- Kebukawa Y., Zolensky M. E., Kilcoyne A. L. D., Rahman Z., Jenniskens P. and Cody G. D. (2014) Diamond xenolith and matrix organic matter in the Sutter's Mill meteorite measured by C-XANES. *Meteorit. Planet. Sci.* **49**, 2095–2103.
- Keller L. P., Messenger S., Flynn G. J., Clemett S., Wirick S. and Jacobsen C. (2004) The nature of molecular cloud material in interplanetary dust. *Geochim. Cosmochim. Acta* **68**, 2577–2589.
- Kilcoyne A. L. D., Tyliczszak T., Steele W. F., Fakra S., Hitchcock P., Franck K., Anderson E., Harteneck B., Rightor E. G., Mitchell G. E., Hitchcock A. P., Yang L., Warwick T. and Ade H. (2003) Interferometer-controlled scanning transmission X-ray microscopes at the Advanced Light Source. *J. Synchrotron Radiat.* **10**, 125–136.
- Le Guillou C., Bernard S., Brearley A. J. and Remusat L. (2014) Evolution of organic matter in Orgueil, Murchison and Renazzo during parent body aqueous alteration: in situ investigations. *Geochim. Cosmochim. Acta* **131**, 368–392.
- Lerotic M., Mak R., Wirick S., Meirer F. and Jacobsen C. (2014) MANTIS: a program for the analysis of X-ray spectromicroscopy data. *J. Synchrotron Radiat.* **21**, 1206–1212.
- Lin Y., Gyngard F. and Zinner E. (2010) Isotopic analysis of supernova SiC and Si<sub>3</sub>N<sub>4</sub> grains from the Qingzhen (EH3) Chondrite. *Astrophys. J.* **709**, 1157–1173.
- Lodders K. and Fegely, Jr., B. (1995) The origin of circumstellar silicon carbide grains found in meteorites. *Meteoritics* **30**, 661–687.
- Matrajt G., Ito M., Wirick S., Messenger S., Brownlee D. E., Joswiak D., Flynn G., Sandford S., Snead C. and Westphal A. (2008) Carbon investigation of two Stardust particles: a TEM, NanoSIMS, and XANES study. *Meteorit. Planet. Sci.* **43**, 315–334.
- Messenger S., Keller L. P., Stadermann F. J., Walker R. M. and Zinner E. (2003) Samples of stars beyond the solar system: silicate grains in interplanetary dust. *Science* **300**, 105–108.
- Nittler L. R., Alexander C. M. O'D., Gao X., Walker R. M. and Zinner E. K. (1994) Interstellar oxide grains from the Tieschitz ordinary chondrite. *Nature* **370**, 443–446.
- Nittler L. R., Amari S., Zinner E., Woosley S. E. and Lewis R. S. (1996) Extinct  $^{44}\text{Ti}$  in Presolar Graphite and SiC: proof of a supernova origin. *Astrophys. J.* **462**, L31–L34.
- Otsu N. (1979) A Threshold Selection Method from Gray-Level Histograms. *IEEE Transactions on Systems, Man, and Cybernetics* **9**, 62–66.
- Paxton A. T., Schilfgaarde M. v., MacKenzie M. and Craven A. J. (2000) The near-edge structure in energy-loss spectroscopy: many-electron and magnetic effects in transition metal nitrides and carbides. *J. Phys. Condens. Mater.* **12**, 729–750.
- Pedregosa F., Varoquaux G., Gramfort A., Michel V., Thirion B., Grisel O., Blondel M., Prettenhofer P., Weiss R., Dubourg V.,

- Vanderplas, Passos A., Cournapeau D., Brucher M., Perrot M. and Duchesnay É. () Scikit-learn: machine learning in Python. *J. Mach. Learn. Res.* **12**, 2825–2830.
- Rauscher T., Heger A., Hoffman R. D. and Woosley S. E. (2002) Nucleosynthesis in massive stars with improved nuclear and stellar physics. *Astrophys. J.* **576**, 323–348.
- Rosenberg R. A., Love P. J. and Rehn V. (1986) Polarization-dependent C(K) near-edge x-ray-absorption fine structure of graphite. *Phys. Rev. B* **33**, 4034–4037.
- Salama F. (2008) PAHs in Astronomy – a review. *Proc. Int. Astron. Union* **4**, 357.
- Savitzky A. and Golay M. J. E. (1964) Smoothing and differentiation of data by simplified least squares procedures. *Anal. Chem.* **36**, 1627–1639.
- Stadermann F. J., Croat T. K., Bernatowicz T. J., Amari S., Messenger S., Walker R. M. and Zinner E. (2005) Supernova graphite in the NanoSIMS: carbon, oxygen and titanium isotopic compositions of a spherule and its TiC sub-components. *Geochim. Cosmochim. Acta* **69**, 177–188.
- Stöhr J. (1992) *NEXAFS Spectroscopy*. Springer-Verlag, Berlin.
- Stroud R. M., Nittler L. R. and Alexander C. M. O'D. (2004) Polymorphism in presolar Al<sub>2</sub>O<sub>3</sub> grains from asymptotic giant branch stars. *Science* **305**, 1455–1457.
- van der Walt S. f., Colbert S. C. and Varoquaux G. I. (2011) The NumPy array: a structure for efficient numerical computation. *Comput. Sci. Eng.* **13**, 22–30.
- van der Walt S., Schonberger J. L., Nunez-Iglesias J., Boulogne F., Warner J. D., Yager N., Gouillart E., Yu T. and scikit-image contributors (2014) scikit-image: image processing in Python. *PeerJ* **2**, e453.
- Woosley S. E. and Weaver T. A. (1995) The evolution and explosion of massive stars. II. Explosive hydrodynamics and nucleosynthesis. *Astrophys. J. Suppl. S.* **101**, 181–235.
- Yabuta H., Mita H., Kobayashi K., Hasegawa N., Kilcoyne, A. L. D. (2010) Direct analysis of Organic Molecules in Carbonaceous Chondrite Through X-Ray Absorption Near Edge Spectroscopy Using Scanning Transmission X-Ray Microscope. *Astrobiology Science Conference 2010: Evolution and Life: Surviving Catastrophes and Extremes on Earth and Beyond*, League City, LPI Contribution No. 1538, p. #5317 (abstr.).
- Yabuta H., Uesugi M., Naraoka H., Ito M., Kilcoyne A. L. D., Sandford S. A., Kitajima F., Mita H., Takano Y., Yada T., Karouji Y., Ishibashi Y., Okada T. and Abe M. (2014) X-ray absorption near edge structure spectroscopic study of Hayabusa category 3 carbonaceous particles. *Earth Planet Space* **66**, 156–166.
- Zega T. J., Nittler L.R., Stroud R. M., Alexander C.M.O'D. and Kilcoyne A. L. D. (2012) Measurement of the Oxidation State of Ti in Solar Hibernite, 43rd Lunar and Planetary Science Conference. Lunar and Planetary Institute, Houston, p. #2338(abstr.).
- Zinner E. (2014) Presolar Grains. In *Treatise on Geochemistry* (eds. K. K. Turekian and H. D. Holland), second ed. Elsevier, Oxford, UK, pp. 181–213.
- Zinner E. and Jadhav M. (2013) Isochrons in presolar graphite grains from Orgueil. *Astrophys. J.* **768**, 100–119.
- Zinner E., Ming T. and Anders E. (1987) Large isotopic anomalies of Si, C, N and noble gases in interstellar silicon carbide from the Murray meteorite. *Nature* **330**, 730–732.
- Zinner E., Wopenka B., Amari S., Anders E. (1990) Interstellar graphite and other carbonaceous grains from the Murchison meteorite: structure, composition and isotopes of C, N, and Ne. Abstracts of the Lunar and Planetary Science Conference XXI, p. #1379(abstr.).
- Zinner E., Amari S., Wopenka B. and Lewis R. S. (1995) Interstellar graphite in meteorites: isotopic compositions and structural properties of single graphite grains from Murchison. *Meteoritics* **30**, 209–226.

Associate editor: Anders Meibom